ABSTRACT

Title of dissertation: DEVLOPMENT AND APPLICATION
                        OF THEORETICAL MODELS
                        FOR ROTATING DETONATION
                        ENGINE FLOWFIELDS

                        Robert Fievisohn, Doctor of Philosophy, 2016

Dissertation directed by: Associate Professor Kenneth H. Yu
                           Department of Aerospace Engineering

As turbine and rocket engine technology matures, performance increases between successive generations of engine development are becoming smaller. One means of accomplishing significant gains in thermodynamic performance and power density is to use detonation-based heat release instead of deflagration. This work is focused on developing and applying theoretical models to aid in the design and understanding of Rotating Detonation Engines (RDEs). In an RDE, a detonation wave travels circumferentially along the bottom of an annular chamber where continuous injection of fresh reactants sustains the detonation wave. RDEs are currently being designed, tested, and studied as a viable option for developing a new generation of turbine and rocket engines that make use of detonation heat release. One of the main challenges in the development of RDEs is to understand the complex flowfield inside the annular chamber. While simplified models are desirable for obtaining timely performance estimates for design analysis, one-dimensional models may not be adequate as they do not provide flow structure information. In this work, a

two-dimensional physics-based model is developed, which is capable of modeling the curved oblique shock wave, exit swirl, counter-flow, detonation inclination, and varying pressure along the inflow boundary. This is accomplished by using a combination of shock-expansion theory, Chapman-Jouguet detonation theory, the Method of Characteristics (MOC), and other compressible flow equations to create a shock-fitted numerical algorithm and generate an RDE flowfield. This novel approach provides a numerically efficient model that can provide performance estimates as well as details of the large-scale flow structures in seconds on a personal computer. Results from this model are validated against high-fidelity numerical simulations that may require a high-performance computing framework to provide similar performance estimates. This work provides a designer a new tool to conduct large-scale parametric studies to optimize a design space before conducting computationally-intensive, high-fidelity simulations that may be used to examine additional effects. The work presented in this thesis not only bridges the gap between simple one-dimensional models and high-fidelity full numerical simulations, but it also provides an effective tool for understanding and exploring RDE flow processes.

DEVELOPMENT AND APPLICATION
OF THEORETICAL MODELS FOR
ROTATING DETONATION ENGINE FLOWFIELDS

by

Robert Fievisohn

Advisory Committee:
Associate Professor Kenneth H. Yu, Chair/Advisor
Professor Arnaud C. Trouve, Dean's Representative
Professor Elaine Oran
Associate Professor Christopher Cadou
Assistant Professor Stuart Laurence

Acknowledgments

First and foremost, I would like to thank my advisor, Dr. Kenneth Yu, for giving me the opportunity to pursue my PhD at the University of Maryland. He brought me on and showed great confidence in my abilities by letting me pursue a research topic of my choosing. With his guidance and support, I was able to conduct research that I am truly proud to have done. I do not think it is possible to have found another advisor who would have been as kind, thoughtful, or helpful as him. It has been a pleasure to work with him.

I would also like to thank the rest of my dissertation committee, Dr. Elaine Oran, Dr. Chris Cadou, Dr. Stuart Laurence, and Dr. Arnaud Trouve for their help and guidance while reviewing my work. I greatly appreciate the amount of time and effort they were willing to dedicate to help me with my research.

I also need to thank the National Science Foundation for supporting this work through the NSF Graduate Research Fellowship Program under grant no. DGE1322106. Having the freedom to pursue a research topic of my choice allowed me to take a risk and work on a truly challenging and interesting topic.

I am also grateful for the help given to me by the UMD Aero department offices including Tom Hurst, Otto Fandino, Michael Jones, LaVita Williams, Rebecca Sarni, and Laura Thorsen. They were always there to offer help and working with them was a pleasure.

I also owe many thanks to my colleagues at the Advanced Propulsion Research Lab. Specifically Jason Burr, Camilo Aguilera, Sammy Park, Jeremy Knittel, and

Table of Contents

List of Figures

List of Symbols

A	area
a	speed of sound
D	detonation wave velocity
F	thrust
g_0	gravitational acceleration at Earth's surface
h	height of RDE annulus
I_{sp}	specific impulse
l	length of RDE domain (average diameter)
P	pressure
M	Mach number
$\dot{m}$	mass flow rate
R	specific gas constant
S	entropy
T	temperature
u	horizontal component of velocity
V	total velocity
w	width of RDE channel
v	vertical component of velocity
Z	acoustic impedance
δ	slip line angle
ϵ	oblique shock angle
γ	ratio of specific heats
θ	flow angle
ρ	density
μ	Mach angle
ψ	mass integral

Subcripts

0	plenum stagnation condition
1	station at throat of injection nozzle
2	station immediately after throat
3	station downstream of throat where properties are uniform
ad	adiabatic flame temperature state
det	state immediately before detonation
e	explosive mixture
$exit$	RDE exit conditions
i	inert mixture
inj	RDE injector conditions
is	isentropically expanded state

lab	laboratory reference frame
x	along x axis
y	along y axis

Chapter 1: Introduction

1.1 Motivation

After more than 60 years of turbine and rocket engine development, increases
in performance are becoming more and more difficult to come by. One idea to in-
crease performance is to change the thermodynamic cycle from a constant pressure
Brayton cycle to a detonation based cycle [1]. Rotating Detonation Engines (RDEs)
are currently being studied and appear to provide a practical and efficient implemen-
tation of detonative combustion [2]. These engines have emerged as an important
concept that, with further development, could provide major increases in jet and
rocket engine performance. An RDE is based on an annular chamber, as shown
schematically in Fig. 1.1. Reactants, such as hydrogen and air, are ignited to create
a detonation which travels around the bottom of the annulus. The detonation is
continuously sustained by the injection of fresh reactants ahead of the wave. Thrust
is generated by expanding the detonation products out the exhaust end of the RDE.
This concept is based on work first performed by Voitsekhovskii whose objective was
to maintain a detonation wave continuously in a circular viewing section for detailed
study [3].

In addition to increasing thermodynamic performance, the relatively small size of the combustion zone in a detonation, compared to traditional constant-pressure combustors, has the potential of reducing the engine length and weight [2]. Finally, the flow behind the detonation wave in an RDE is supersonic; therefore, acceleration of the flow only requires area divergence and eliminates the need for a geometric throat [2]. Before any of these potential benefits can be realized in a practical system, there are many challenges to overcome, such as heat losses, injector dynamics, and understanding the complex flow structure that occurs within the annulus [2, 4–6].
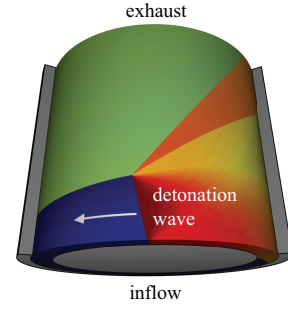
Figure 1.1: Schematic of an RDE showing a temperature contour map.

Current understanding of RDEs comes primarily from experimental and numerical results. These can be costly and time-consuming when attempting to explore the design space for a proposed engine. Ideally, a simple, fast model that accurately captures the physics is required to generate a design space that can guide what experiments and simulations are actually necessary when designing an engine. The simple models that have been developed generally have to disregard some flow structures or make educated guesses about them. A simple model that can correctly and accurately capture the relevant flow structures and physics would be of great value to the research community and is the focus of this work.

1.2   Objective

The primary objective of this work is develop a reduced order model of the RDE flowfield. The goal is to accurately and correctly capture the relevant flow physics using a computationally cheap model that is ideally suited to conducting large parametric performance studies. Unlike previous reduced order models, this model will accurately capture two-dimensional effects such as 1) the curved oblique shock wave, 2) detonation inclination, 3) exit swirl, 4) counter-flow, and 5) the varying pressure along the inflow boundary.

The reduced order model solves the RDE flowfield in the wave-fixed reference frame using a shock-fitted numerical solution. Discontinuities such as the detonation, oblique shock, slip lines, and inflow boundary are modeled analytically. This significantly reduces the computational cost normally associated with resolving these features. The Method of Characteristics (MOC) is chosen to numerically solve the flowfield resulting in an extremely fast and accurate solution.

Once the model has been developed and validated, a large parametric study is performed to examine an ideal RDE as a means of demonstrating the potential of this method. The performance data is then analyzed to determine which parameters are important in maximizing performance. Simplified relations are also developed based on the parametric data to provide back-of-the-envelope performance estimates for RDEs.

Specifically, this work will include the following:

- Development of a reduced order model of the RDE flowfield using a Method

of Characteristics approach.

- The development of new boundary conditions for MOC specifically created for RDEs.

- Improved algorithms for rotational MOC in regions with large entropy gradients and non-constant flow ahead of an oblique shock wave.

- Validation of the reduced order model with comparisons to traditional numerical simulations.

- A large parametric study of an ideal RDE using the developed model to determine which parameters have the largest impact in determining performance.

- Simplified design rules for an RDE based on data from the parametric study to aid in the design process.

1.3 Scope

The scope of this work covers the important physical processes present in an idealized RDE. This idealized RDE setup ignores the deflagration, viscous and heat conduction losses, and three-dimension curvature effects. Instead, the focus is on the large scale flow structures such as the detonation and oblique shock, as well as the expansion of the detonation products to produce thrust and allow for the injection of reactants ahead of the next wave.

Once a fundamental understanding of the important processes in an RDE is achieved. A reduced order model based on a shock-fitted method of characteristics

solution is created. This will require the development of new boundary conditions, new marching methods, and new algorithms to extend the method of characteristics in order to handle RDE physics.

After the creation of a reduced order model, a large parametric study is conducted along with a dimensional analysis. Results from the parametric study are compared with the dimensional analysis to confirm the validity of the reduced order model. Additionally, the dimensional analysis and parametric study are used to estimate functional relationships between the independent and dependent parameters in an RDE.

Chapter 2:   Background

This chapter provides an overview of the material required to put the subsequent chapters in context. Summaries of detonation based propulsion, rotating detonation engine research and models, and detonations with compressible boundaries are provided. This gives an overview of the basis for the reduced order model as well as its place within RDE research.

2.1   Detonation Based Propulsion

The idea for using detonation based propulsion in aerospace applications has been around since at least the 1940's. For the most part, the idea was not seriously pursued at the time due to the difficulty in minimizing the losses associated with a detonation based cycle [7]. Improvements in other areas such as compressors, turbines, and materials were easier to come by in the quest to increase performance.

Starting in the early 1990's, detonation based propulsion received renewed interest due to the increasing maturation of turbine engine technology. Detonation combustion was seen as a potential avenue for significant performance increases which were becoming harder to come by with each new generation of engines.

The research of the 1990's was focused on the development of the Pulse Detonation Engine (PDE). A PDE is simply a tube that is filled with a detonable mixture that is then ignited to produce thrust. This results in a highly unsteady

Figure 2.1: First flight of a PDE powered aircraft.

process characterized by a cylce of 1) fill, 2) ignite, 3) detonation, 4) purge, and 5) repeat. It was found that the ignition and subsequent deflagration-to-detonation transition (DTT) was a major source of losses. In 2008, work on PDEs culminated in a flight test of a heavily modified Rutan Long-EZ [5,8] (see Fig. 2.1 [9]). Afterwards, research shifted mainly to Rotating Detonation Engines (RDEs) as an alternative to PDEs that did not suffer from low operating frequencies or the requirement to initiate a detonation every cycle [4]. This work focuses exclusively on modeling RDEs to provide a reduced order model for parametric performance studies.

For completeness, there are two other concepts in the literature for achieving detonation based propulsion. The first is the Standing Detonation Wave Engine. This is a ramjet-type engine where the flow velocity in the combustor is kept at the detonation wave velocity so that a detonation sits in the combustor. A basic analysis of this type of engines shows that it is less efficient than a traditional constant-pressure ramjet and was never seriously pursued [7,10].

The second concept is known as an Oblique Detonation Wave Engine. This is similar to the Standing Detonation Wave Engine but an oblique detonation wave is stabilized in the combustor instead of a normal detonation wave. This concept would be used in a scramjet-type engine. It is less efficient than a constant-pressure

combustor but the losses are not as bad as what is seen in a Standing Detonation Wave Engine. The concept has not been dismissed out of hand since there is evidence that the short reaction zone could provide some benefit by reducing engine length and weight in a scramjet [11].

2.1.1   Detonation Thermodynamics

A brief overview of detonation thermodynamics is important in understanding the reason behind the interest in detonation based propulsion. It is also important in understanding why certain ideas, such as Pulse Detonation Engines (PDEs) and Rotating Detonation Engines (RDEs), are pursued over ideas such as the Standing Detonation Wave Engine.

To start with, the simplest analysis of a detonation wave is accomplished using Chapman-Jouguet (CJ) theory. This theory models a one-dimensional, planar detonation wave as an infinitely thin shock with heat release in the wave-fixed reference frame as shown in Fig. 2.2. Assuming a perfect gas with equal specific heat capacities between the products and reactants, the conservation equations for an adiabatic, inviscid fluid across an infintely thin wave are given by

$$\rho_1 u_1 = \rho_2 u_2 \tag{2.1}$$

$$\rho_1 u_1^2 + P_1 = \rho_2 u_2^2 + P_2 \tag{2.2}$$

$$c_p T_1 + \frac{u_1^2}{2} = c_p T_2 + \frac{u_2^2}{2} - q \tag{2.3}$$

where q is the chemical heat release. Combining the mass and momentum equations
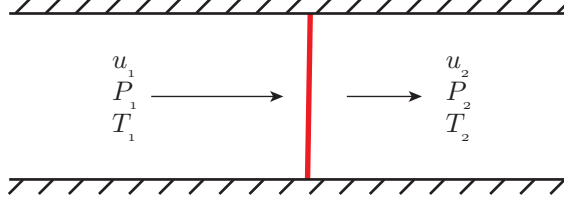
Figure 2.2: Illustration of Chapman-Jouguet detonation wave in the wave-fixed reference frame.

gives the equation for the Rayleigh line [12] given by

$$\frac{P_2}{P_1} = (1 + \gamma M_1^2) - (\gamma M_1^2)\frac{\nu_2}{\nu_1}. \tag{2.4}$$

Combining the mass, momentum, and energy equations gives the Rankine-Hugoniot line [12] given by

$$\frac{P_2}{P_1} = \frac{\frac{\gamma+1}{\gamma-1} - \frac{\nu_2}{\nu_1} + 2\frac{q}{P_1\nu_1}}{\frac{\gamma+1}{\gamma-1}\frac{\nu_2}{\nu_1} - 1}. \tag{2.5}$$

The points where the Rayleigh line is tangent to the Hugoniot are known as the upper and lower Chapman-Jouguet points as shown in Fig. 2.3. The upper CJ point corresponds to a detonation and the lower CJ point corresponds to a deflagration. The entropy along the Hugoniot is given by

$$\frac{s_2 - s_1}{R} = \frac{1}{\gamma - 1}\ln\frac{P_2}{P_1} + \frac{\gamma}{\gamma - 1}\ln\frac{\nu_2}{\nu_1}. \tag{2.6}$$

This is plotted in Fig. 2.4. It can be readily seen that an entropy minimum occurs at the upper CJ point that represents a detonation. It is this entropy minimum that shows that a detonation is a thermodynamically more efficient burning process than a deflagration wave.

When analyzing a propulsion system, it is important to look at the flow processes through the entire engine. To accomplish this, stagnation Hugoniot analysis
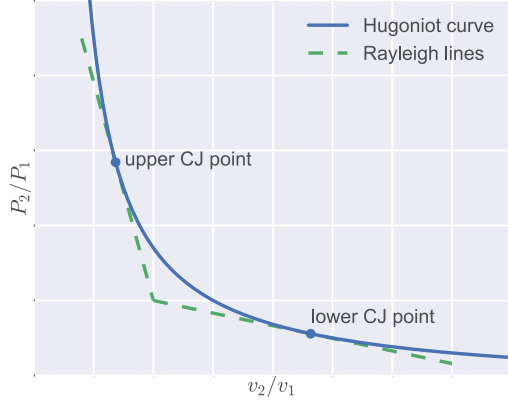
Figure 2.3: Rayleigh and Hugoniot lines for a CJ detonation.
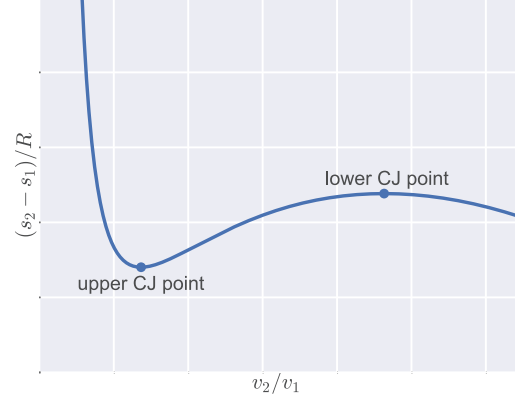
Figure 2.4: Entropy variation along the Hugoniot.

was created by Wintenberger and Shepherd [10]. This analysis may be used to analyze a Standing Detonation Wave Engine which uses a steady detonation wave that is stabilized in a combustor where the flow velocity is equal to the detonation velocity. The stagnation Hugoniot analysis takes into account the freestream stagnation pressure and the pressure ahead of the combustion wave. For a traditional constant-pressure system such as a ramjet, the flow velocity in the combustor is very low and nearly all of the freestream stagnation pressure is recovered. For a Standing Detonation Wave Engine, the velocity in the combustor is very high and little to no stagnation pressure is recovered. The analysis shows that recovering the stagnation pressure is critical to having an efficiently operating engine and that the traditional constant-pressure ramjet is vastly more efficient than the detonation based ramjet.

The equation for the stagnation Hugoniot [10] is given by

$$\frac{P_2}{P_1} = 1 + \frac{2\gamma}{\gamma - 1}\left(1 - \frac{\nu_2}{\nu_1}\right)\left[\frac{1 + \frac{q}{c_p T_t} - \frac{\nu_2}{\nu_1}}{\frac{\gamma+1}{\gamma-1}\left(1 - \frac{\nu_2}{\nu_1}\right)\frac{\nu_2}{\nu_1} + \frac{\nu_2}{\nu_1} - \left(1 + \frac{q}{c_p T_t}\right)}\right] \qquad (2.7)$$

where T_t is the freestream stagnation temperature. The stagnation Hugoniot is
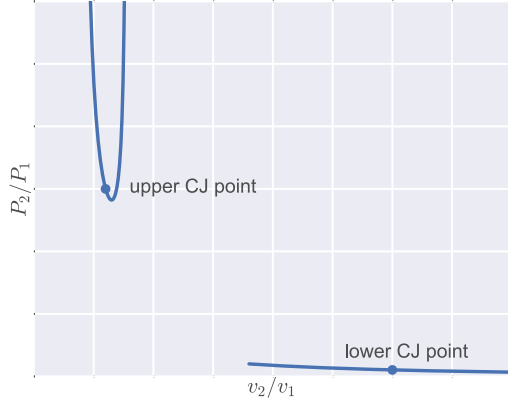
Figure 2.5: Stagnation Hugoniot in the P-ν plane.
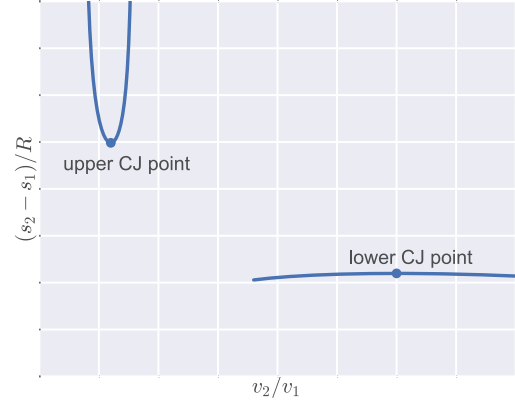
Figure 2.6: Entropy variation along the stagnation Hugoniot.

plotted in Fig. 2.5 and the entropy variation is plotted in Fig. 2.6. The upper CJ point corresponds to the detonation solution that would be seen in an ideal Standing Detonation Wave engine. The lower CJ point corresponds to a deflagration and is similar to what would be seen in an ideal ramjet. By not recovering the stagnation pressure before combustion, the Standing Detonation Wave Engine ends up being less efficient.

It is important to note that the stagnation Hugoniot only applies to steady combustion systems such as ramjets and Standing Detonation Wave Engines. An unsteady combustion system, such as a PDE or RDE, should in theory be able to recover the freestream stagnation pressure before combustion and realize the thermodynamic benefits of detonative over deflagrative combustion. An illustration of the various cycles discussed is given in Fig. 2.7. It can be seen that a steady detonation process (ZND cycle) is less efficient than the equivalent steady deflagration process (Brayton cycle). However, the unsteady ZND cycle is more efficient than either. The unsteady Humphrey cycle which represents a constant volume combus-
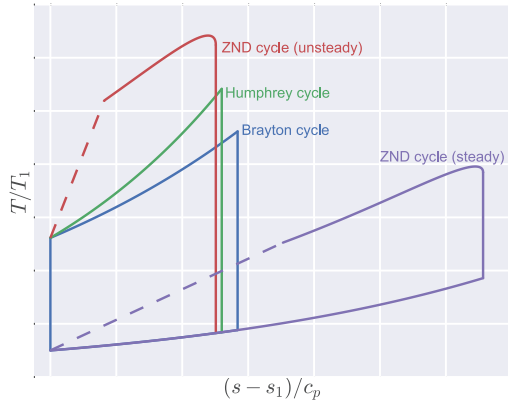
Figure 2.7: T-s plots of various thermodynamic cycles.
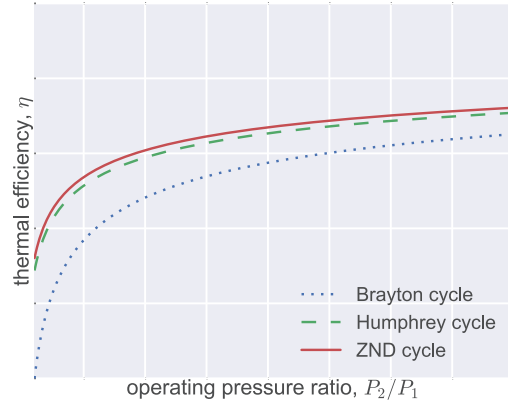
Figure 2.8: Thermal efficiency of various cycles vs. the operating pressure ratio.

tion process with constant pressure heat rejection is also shown due to its similarities with the unsteady detonation cycle.

Figure 2.8 shows the thermal efficiency of the Brayton, Humphrey, and unsteady detonation cycles versus the operating pressure ratio of an engine. For low operating pressures, the Humphrey and ZND cycles offer far greater thermal efficiency than the constant pressure Brayton cycle. At higher operating pressures, the differences between the various cycles decreases. This implies that detonation based propulsion could provide larger efficiency increases for engines with low operating pressures. This could include augmentors or engines that spend large amounts of time in low power or idle modes. High operating pressure engines, such as rockets and modern jet engine combustors, would see less benefit. However, this does not take into account potential weight savings due to having a much smaller flame brush or vastly increased flame speeds.

2.2 Rotating Detonation Engines

The focus of this work is on Rotating Detonation Engines (RDEs). The RDE concept was first put forward by Voitsekhovskii in 1960 who was attempting to maintain a detonation wave for study [3]. This device pushed a pre-mixed detonable mixture through a radial slit into a viewing area where a detonation was initiated and could be maintained for study. A schematic of the device is shown in Fig. 2.9. The detonation products then exit the viewing section radially. This device was designed to study detonations and was not designed with propulsion in mind. In 1966, Nicholls et. al. attempted to create a propulsion device based on this idea that they called a Rotating Detonation Wave Rocket Motor [13]. Their device was designed to examine the feasibility of this concept as an engine and to also understand combustion instabilities in liquid rocket motor engines. Unfortunately, they were unable to sustain continuous operation but did put forward analyses and data that would be useful in designing future RDEs. After the work done by Nicholls et. al., research in the U.S. on RDEs stopped for several decades. However, in Russia, research into RDEs continued and is ongoing today. In the 1990's through 2010, interest in Pulse Detonation Engines (PDEs) led to a greater understanding of detonation phenomena. Starting in the mid-00's, this increased understanding led to the development of working RDEs for experimental study. Two ways of incorporating RDEs into current propulsion concepts are shown in Figs. 2.10 and 2.11 [14]. Figure 2.10 shows how an RDE may be used in a ramjet-type system. Figure 2.11 shows how an RDE may replace the combustor in a gas turbine engine.

1 Annular Channel
2 Upper Transparent Wall
  of the Annular Channel
  Made of Plastic Glass
3 Photorecorder
4 Valve
5 Gas Supply Reservoir with
  Initial Mixture
6 Tank Which Receives the
  Burned Gas After Being
  Initially Pumped Down to
  the Correct Pressure
7 Direction of the Starting
  Impulse
8 Central Channel Which Con-
  ducts the Initial Mixture to
  the Detonation Annulus
9 Exhaust Manifold
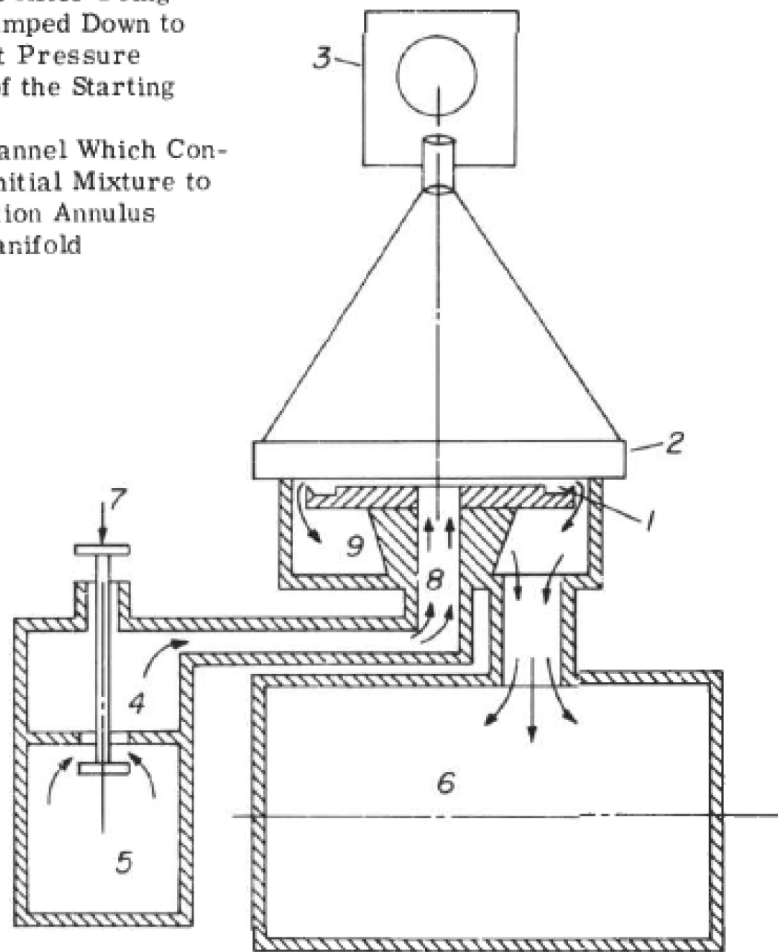
Figure 2.9: Schematic of Voitsekhovskii's maintained detonation device. From [3].
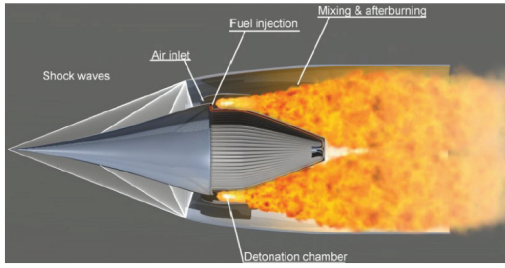
Figure 2.10: Schematic of an RDE based ramjet. From [14].
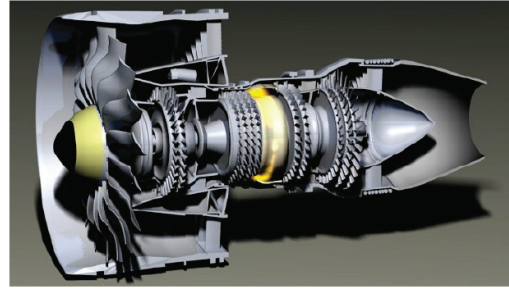
Figure 2.11: Schematic of an RDE based turbofan. From [14].

There are now many research programs on RDEs in the U.S., Russia, France, China, South Korea, Japan, Poland, and others. Experimental, computational, and analytical results from these groups will be explored in subsequent sections.

2.2.1 Overview of RDE Flowfield

Current understanding of the RDE flowfield comes primarily from experimental and numerical results. For example, Fig. 2.12, taken from a CFD simulation of an RDE flowfield [15], shows a detonation propagating into premixed, fresh reactants injected ahead of the detonation front. The products then expand and a slip line is formed between the new products and the products of the previous detonation that have gone through an oblique shock. A Kelvin-Helmholtz instability forms along the slip line as well. A deflagration wave may or may not form between the injected reactants and detonation products depending upon the local equivalence ratio. The deflagration that occurs is sometimes known as contact surface burning [6]. A secondary shock may also form in the detonation products, depending on the flow conditions. Note that in experimental studies, reactants are not premixed
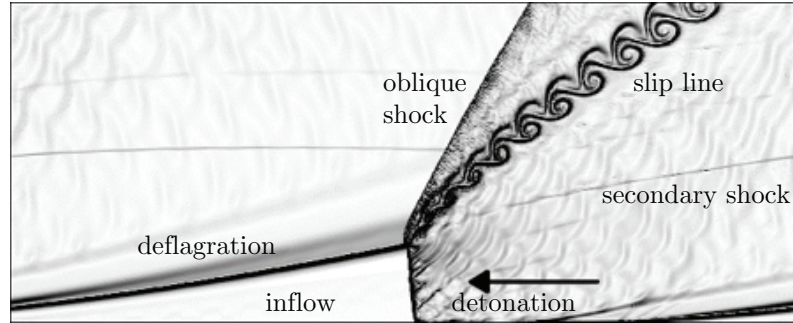
Figure 2.12: Numerical schlieren of an RDE simulation. From [15].

and mixing occurs in the inflow region ahead of the detonation.

2.2.2 Experimental Studies

After the initial experimental work by Voitsekhovskii in Russia and Nichols in the U.S. during the 1960's, research into rotating detonations continued in Russia and is still being studied today. Bykovskii and Mitrofanov looked at a annular geometry similar to what is shown in Fig. 1.1 with acetylene-oxygen and propane-oxygen mixtures to study the basic science behind rotating detonations [16]. Additional work by Bykovskii et. al. looked at radial annular chambers similar to Voitsekhovskii's initial device shown in Fig. 2.9 [17]. There were different chamber types studied where the inflow was injected radially outwards similar to Voitsekhovskii and one that injected the reactants radially inwards. Bykovskii and Vedernikov also studied a device where a detonation propagated around a cylinder with no outer walls that was sustained by a radial outflow of reactants [18].

The previous studies conducted by Bykovskii and others used pure oxygen. In 1997, Bykovskii, Mitrofanov, and Vedernikov achieved a rotating detonation using air as an oxidizer using a radial annular geometry where the reactants were injected

16
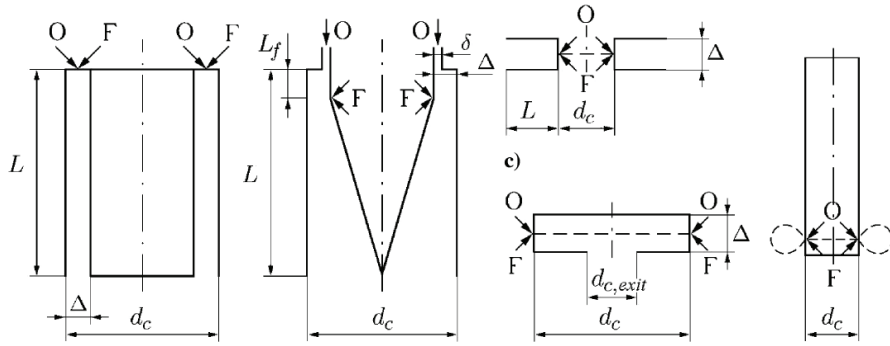
Figure 2.13: Various geometries of Russian RDEs. From [2].

radially inwards [19]. After this, Bykovskii, Zhdan, and Vedernikov demonstrated fuel-air RDEs using annular geometries that are similar to what would be seen in an aerospace application [2, 20–22]. Figure 2.13 shows some geometries studied by Bykovskii and others for their initial experiments into RDEs. Bykovskii et. al. also conducted studies into rocket-type RDEs that examined annular geometries and expanding annular geometries [23–27]. Additional experimental studies were conducted into RDEs that injected fuel at high enough pressure to entrain outside air for combustion [28–32] and the effect of using air to dilute the detonation products [33]. Lastly, the effect of heat flux to the combustor walls [34,35], noise and vibration [36], and detonation initiation [37] has also been studied by Bykovskii et. at.

These extensive studies conducted by Bykovskii have provided some key takeaways for the research community. First and foremost, the structure of the flowfield was extensively described and documented and an illustration of it may be seen in Fig. 2.14
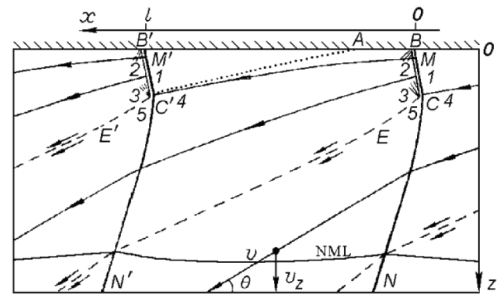
Figure 2.14: Illustration of RDE flowfield. From [2].

17

[2]. Note that their coordinate system has

the inflow coming from the top and the detonation is progressing from left to right.

They also examined how physical geometry, mixture properties, and mass flow affected RDE operation. Operating regimes for both rocket-type and airbreathing

RDEs were defined in order to provide starting points for future designs [2]. Lastly,

an important stability criteria states that the detonation height must be approximately $(12 \pm 5)\lambda$ in order to successfully propagate a detonation around the annulus [2]. Note that λ is the detonation cell width.

Since 2010, the U.S. has built and operated many RDEs. The first set of RDEs built and tested consisted of a 3 inch diameter RDE [39], a 6 inch diameter RDE [40], and a 22 inch diamter RDE [41]. Additionally, experiments looking at heat transfer [42] and the performance of a converging-diverging nozzle [43] have been looked at. Of

Figure 2.15: Chemiluminescense image of RDE flowfield. From [38].
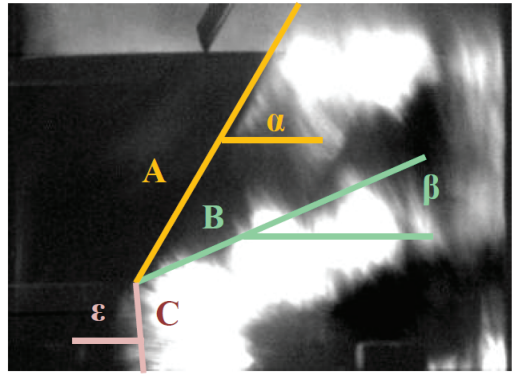
particular relevance to this work, a RDE was designed with a quartz outerbody so

that the RDE flowfield could be directly observed through chemiluminescence [38].

An image from the quartz outerbody is shown in Fig. 2.15 [38]. It clearly shows

the detonation wave which is inclined slightly forward and an oblique shock being

dragged around. It is also possible to see the slip line.

Lastly, there are robust experimental RDE programs in both Poland and

France that deserve mention. In Poland, Wolański et. al. have conducted many

RDE experiments for both rocket-type RDEs [44] and airbreathing RDEs [44]. France also has an RDE program with working devices that has confirmed many of the Russian results [45].

2.2.3   Computational Studies

Many computational studies have been conducted to understand the physics that occur within an RDE and how they affect performance and operation. Due to the difficulty of making measurements within the RDE environment, computational fluid dynamics (CFD) has been an invaluable tool for filling in some of the gaps in experimental knowledge.

The simplest RDE simulations are unsteady, two-dimensional Euler simulations. If the RDE channel width is small compared to the radius of curvature, an annular channel may be approximated as two-dimensional with periodic boundary conditions. Most of these simulations assume the injected mixture is premixed to reduce computational requirements [15, 46–55]. It should also be noted that the CFD model used by Zhdan et al. is capable of performing quasi two-dimensional simulations [52]. These simulations provided a detailed look at the RDE flowfield seen in Fig. 2.12. The effects of various geometric parameters have also been examined [15] along with nozzling of the RDE channel [56]. Studies on different inflow geometries and the effects of the detonation wave on an injector plenum have also been examined [49–51]. The role of mixing has also been examined [57–59]. Recently, increases in computer power have allowed for the inclusion of turbulence [60]

and full three-dimensional simulations [56, 61–63].

At a minimum, the computational cost of these models normally requires several hours of run time on a supercomputer. Some of the larger three-dimensional simulations can take weeks or even months. Due to the large computational cost of CFD simulations, these models are best suited to examining the physics in detail and not for large parametric studies to build out a design space for an engine. The goal of this work is to build a model that can reproduce the results of the simple, two-dimensional simulations with premixed reactants and ideal injection systems.

2.2.4   Analytical Studies

Simplified and reduced order models have been developed to determine RDE performance and conduct parametric studies. Nordeen et. al. used a modified ZND model to take into account the rotating reference frame of the detonation wave in an RDE [64]. This model is a analytical one-dimensional model that takes into account two-dimensional effects through a velocity transformation. Kaemming et. al. developed a reduced order model of the multiple thermodynamic cycles that occurs within an RDE to estimate performance [65]. Mizener and Lu also created an analytical control-volume approach to estimating RDE performance [66]. Lastly, Paxson developed a CFD simulation that solves the RDE flowfield in the wave-fixed reference frame on a relatively coarse grid to generate solutions faster than more refined codes [67]. With the exception of the Paxson CFD solver, these models require empirical results or educated guesses from higher-fidelity simulations. The

goal of this work is to present a two-dimensional model that does not require any previous knowledge except for a basic understanding of the shock structure in an RDE that is suitable for parametric studies.

2.3   Detonations with Compressible Boundaries

The basis of the current work can be traced back to research performed in the 1960s. Several researchers investigated a flow similar to that seen in RDEs [68–71]. They performed experiments in a thin rectangular channel with a detonable mixture on the bottom and an inert mixture on top. Early experiments allowed diffusion to occur between the two mixtures [69], while later experiments used a thin film to separate the gases [68]. Figure 2.16, is a spark photograph of an experiment to visualize a detonation bounded by an inert gas. Analytical methods for calculating the oblique shock and slip line angles were given by Sommers and Morrison [69]. Dabora extended this analysis to include losses through the
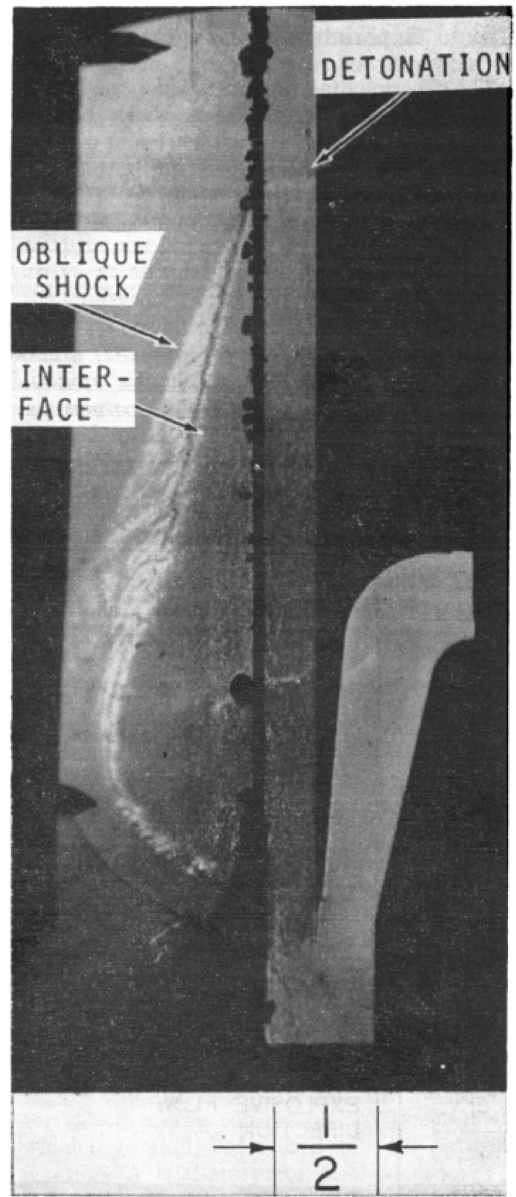
Figure 2.16: Experimental image of a detonation wave bounded by an inert gas. From [68].
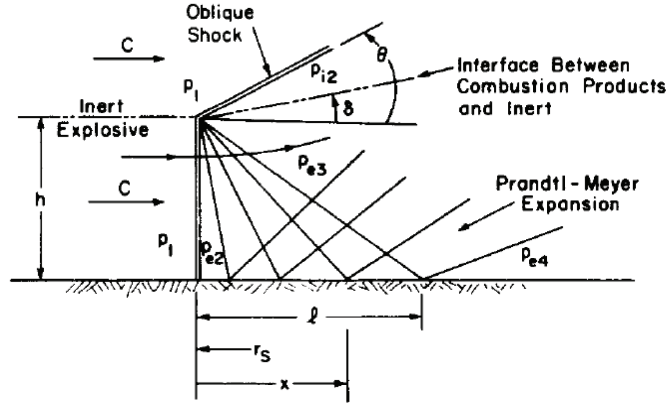
Figure 2.17: Diagram of detonation-inert interaction. From [70].

reaction zone to estimate the velocity deficit

and detonability limits [68]. A more rigorous

method for estimating the velocity deficit was then given by Fujiwara and Tsuge [71].

Sichel and Foster extended the analytical solution of Sommers and Morrison to cal-

culate the pressure distribution on the bottom surface behind the detonation wave

using the method of characteristics (MOC) [70]. A diagram of their system is given

in Fig 2.17.

The focus of this paper is to extend the ideas of Sichel and Foster to an RDE.

Examination of Fig. 2.17 and Fig. 2.12 show many similarities of the gross shock

structure. In this work, the major flow structures, i.e., the oblique shock, slip line,

and centered expansion fan, are calculated analytically using the methodology of

Sommers and Morrison by assuming that the inert gas bounding the detonation

consists of detonation products from the previous wave. The resulting flow struc-

tures are then used as the basis for a shock-fitted MOC solution. This leads to the

development of a simplified, steady-state 2D RDE model suitable for large paramet-

ric studies.

Chapter 3:   Analytical Modeling of RDE Flow Structures

This chapter discusses the analytical models that are used in the reduced order model being developed. These analytical models describe discontinuities in the flowfield. By modeling discontinuities analytically, a shock-fitted model may be developed. This greatly decreases the computational cost when compared to a shock-capturing model which requires high-resolution grids to resolve the discontinuities. The discontinuities in the RDE flowfield that are modeled analytically are the planar detonation wave, the oblique shock, the slip lines, and the injector.

3.1   Analytical Model of the Detonation-Oblique Shock Structure

Figure 3.1 is an idealized model of a propagating detonation bounded by an inert gas in the wave-fixed reference frame. Sommers and Morrison noted that this system resembles the interaction of a shock wave incident on a free boundary and may be solved in a similar manner [69]. Figure 3.2 is an extension of Fig. 3.1 to an RDE flowfield. The inclusion of reactants being injected in front of the detonation adds a vertical component of velocity ahead of the wave. This inclines the detonation and generates of a second expansion fan that emanates from the bottom of the detonation and turns the flow parallel to the wall. This is caused by the high pressure
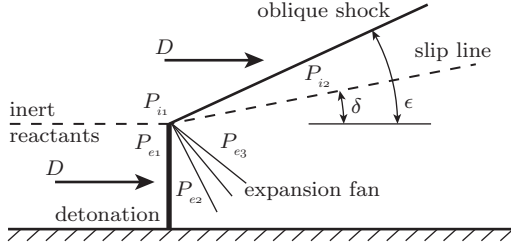
Figure 3.1: Ideal detonation-inert model.
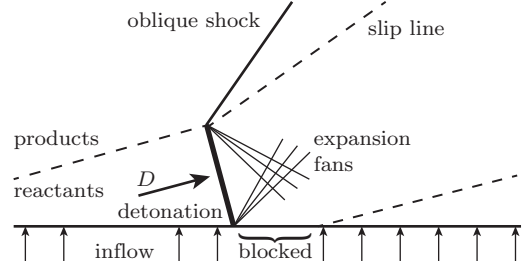
Figure 3.2: Ideal RDE model.

detonation products blocking inflow from occurring until the pressure relaxes below a certain point. Note that this model assumes that the high pressure does not cause any detonation products to flow back into the injection system (i.e., no backflow). Lastly, the ideal RDE flowfield model assumes there is no deflagration wave along the contact surface between the reactants and products.

The simpler model of a detonation bounded by an inert gas in Fig. 3.1 is analyzed first to provide insights into the RDE model in Fig. 3.2. Following Fig. 3.1, if the CJ solution is provided, D and P_{e_2} are known. The subscript, i, stands for the inert bounding gas and subscript, e, stands for the explosive mixture. Since $P_{e_3} = P_{i_2}$, there are now only three unknowns: δ, ϵ, and P_{e_3} (or P_{i_2}). In the following analysis, M_{e_3} is used in place of P_{e_3}, since they are related isentropically. The relationship between δ and ϵ is given by the oblique shock relation:

$$\tan \delta = 2 \cot \epsilon \left[\frac{M_{i_1}^2 \sin^2 \epsilon - 1}{M_{i_1}^2 (\gamma_i + \cos 2\epsilon) + 2} \right]. \tag{3.1}$$

Since both temperature and composition can vary across the interface, $M_{i_1} \neq M_{e_1}$. The relationship between δ and M_{e_3} is given by

$$\delta = \nu(M_{e_3}) - \nu(M_{e_2}) \tag{3.2}$$

24

where $\nu(M)$ is the Prandtl-Meyer function. The pressure across the oblique shock is given by

$$\frac{P_{i_2}}{P_{i_1}} = 1 + \frac{2\gamma_i}{\gamma_i + 1}(M_{i_1}^2 \sin^2 \epsilon - 1). \tag{3.3}$$

The pressure across the expansion wave is given by the isentropic relation

$$\frac{P_{e_2}}{P_{e_3}} = \left[\frac{1 + \dfrac{\gamma_{e_2} - 1}{2} M_{e3}^2}{1 + \dfrac{\gamma_{e_2} - 1}{2} M_{e2}^2} \right]^{\gamma_{e_2}/(\gamma_{e_2} - 1)}. \tag{3.4}$$

The pressures on either side of the interface are equal and may be related by the expression:

$$\frac{P_{i_2}}{P_{i_1}} = \left(\frac{P_{e_1}}{P_{i_1}} \right) \left(\frac{P_{e_2}}{P_{e_1}} \right) \left(\frac{P_{e_3}}{P_{e_2}} \right), \tag{3.5}$$

where P_{e_2}/P_{e_1} is the pressure ratio across a detonation wave. In this work the detonation solution may be provided by either 1-γ, 2-γ, or equilibrium Chapman-Jouguet models that are described later in this chapter. There are now three unknowns: δ, ϵ, and M_{e_3} in three equations: (3.1), (3.2), and (3.5). These equations may then be solved simultaneously using a nonlinear equation solver.

3.1.1 Applicability of Shock Structure Model

Examining Fig. 2.12 shows a secondary shock that is not present in the previous analysis. This secondary shock occurs if the oblique shock becomes detached. The subsonic region behind a detached shock would necessitate the use of a transonic patch to make possible a method of characteristics solution. It would be simpler to model the flow without this secondary shock; therefore, the system of equations governing the detonation-oblique shock interaction is analyzed to determine when

the oblique shock detaches to determine the scope of where this model is valid. The system is also analyzed to determine when the flow behind the oblique shock becomes sonic which would rule out the possibility of performing a method of characteristics solution as well.

The parameters of the system defined by equations (3.1), (3.2), (3.5), and Fig. 3.1 are a function of the ratio of acoustic impedances between the inert and explosive layers [69], where the acoustic impedance is defined as

$$Z = \rho a = \frac{\gamma P}{a}. \tag{3.6}$$

Figure 3.3 shows the relationship between the oblique shock angle and the ratio of the acoustic impedances in an inert versus an explosive medium. A simple 1-γ model for stoichiometric hydrogen-air [72] is used to perform the detonation calculation. Across the detonation wave, the composition of the gas and the heat capacities may change. Elsewhere, a frozen, calorically perfect gas is assumed. At a certain point, the shock can become detached. This point may be found with the following equation for the maximum oblique shock angle:

$$\sin^2 \epsilon_{max} = \frac{1}{\gamma_i M_{i_1}^2} \left[\frac{\gamma_i + 1}{4} M_{i_1}^2 - 1 + \sqrt{(\gamma_i + 1) \left(1 + \frac{\gamma_i - 1}{2} M_{i_1}^2 + \frac{\gamma_i + 1}{16} M_{i_1}^4 \right)} \right]. \tag{3.7}$$

There is also the possibility that the flow becomes sonic or subsonic behind the oblique shock. This oblique shock angle where this occurs is given by:

$$\sin^2 \epsilon^* = \frac{1}{\gamma_i M_{i_1}^2} \left[\frac{\gamma_i + 1}{4} M_{i_1}^2 - \frac{3 - \gamma_i}{4} + \sqrt{(\gamma_i + 1) \left(\frac{9 + \gamma_i}{16} - \frac{3 - \gamma_i}{8} M_{i_1}^2 + \frac{\gamma + 1}{16} M_{i_1}^4 \right)} \right]. \tag{3.8}$$
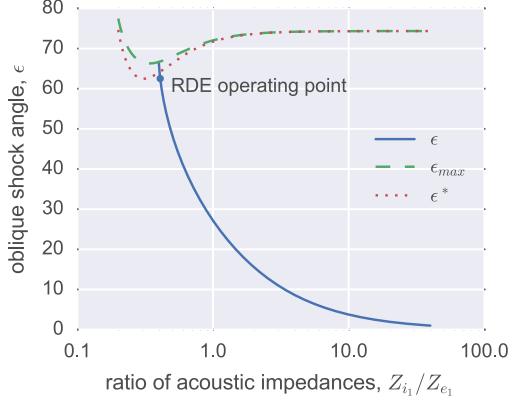
Figure 3.3: ϵ vs. Z_{i_1}/Z_{e_1}.
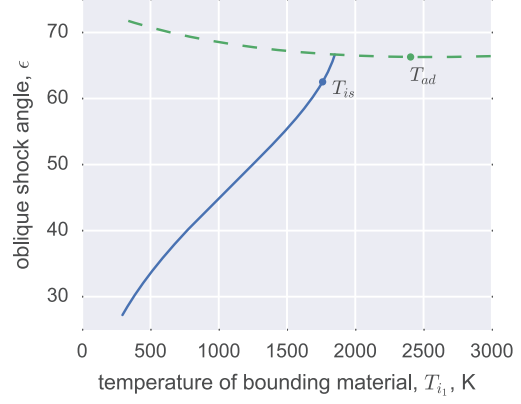
Figure 3.4: ϵ vs. T_{i_1}.

To examine the behavior of an RDE, the inert gas bounding the detonation is assumed to consist of detonation products that have been isentropically expanded down to the initial pressure of the reactants in front of the detonation. Therefore, the temperature of the inert gas is given by

$$T_{i_1} = T_{e_2} \left(\frac{P_{i_1}}{P_{e_2}} \right)^{(\gamma_i - 1)/\gamma_i} \tag{3.9}$$

where $\gamma_i = \gamma_{e_2}$. According to Fig. 3.3, for a stoichiometric hydrogen-air detonation at standard conditions, the oblique shock wave should remain attached and the post-shock flow supersonic.

A closer examination of Fig. 2.12 shows that the point where the detonation and oblique shock intersect resides in the deflagration wave formed between the reactants and detonation products. If the temperature of the bounding detonation products is varied as shown in Fig. 3.4, the oblique shock wave would detach at temperatures less than the adiabatic flame temperature. Therefore, the deflagration wave appears to be the most likely reason for the formation of the secondary shock. The idealized model developed here disregards the deflagration wave that forms, so

27

modeling the secondary shock is unnecessary and may be ignored.

3.2 Chapman-Jouguet Detonation Waves

The ideal RDE model being developed represents the detonation as an infinitely thin, planar wave. The detonation velocity and jump conditions across this wave are required and are determined using Chapman-Jouguet theory. These jump conditions are provided using either a 1-γ, 2-γ, or equilibrium CJ solution. This section will detail the calculation of the detonation velocity and jump conditions given the state of the reactants ahead of the wave.

3.2.1 Simple 1 and 2-γ Models

The CJ detonation solution for a 2-γ mixture is presented in this section. The 1-γ may be found by assuming that $\gamma_1 = \gamma_2$ in the following equations. Referencing Fig. 2.2, the conservation equations across the wave where the reactants and products may have different molecular weights and specific heat capacities are given by:

$$\rho_1 u_1 = \rho_2 u_2 \tag{3.10}$$

$$\rho_1 u_1^2 + P_1 = \rho_2 u_2^2 + P_2 \tag{3.11}$$

$$c_{p,1} T_1 + \frac{u_1^2}{2} = c_{p,2} T_2 + \frac{u_2^2}{2} - q. \tag{3.12}$$

The equation for the Rayleigh line is given by:

$$\frac{P_2}{P_1} = (1 + \gamma_1 M_1^2) - (\gamma_1 M_1^2)\frac{\nu_2}{\nu_1} \tag{3.13}$$

and the equation for the Hugoniot is given by:

$$\frac{P_2}{P_1} = \frac{\frac{\gamma_1+1}{\gamma_1-1} - \frac{\nu_2}{\nu_1} + 2\frac{q}{P_1\nu_1}}{\frac{\gamma_2+1}{\gamma_2-1}\frac{\nu_2}{\nu_1} - 1}. \tag{3.14}$$

From Chapter 2, the CJ solutions correspond to the points when the Rayleigh line is tangent to the Hugoniot. Since the detonation solution is desired, only the upper CJ point is given here. The Mach number that corresponds to the CJ detonation solution is given by

$$M_{CJ} = \sqrt{\mathcal{H} + \frac{(\gamma_1+\gamma_2)(\gamma_2-1)}{2\gamma_1(\gamma_1-1)}} + \sqrt{\mathcal{H} + \frac{(\gamma_2-\gamma_1)(\gamma_2+1)}{2\gamma_1(\gamma_1-1)}} \tag{3.15}$$

where the nondimensional energy release, $\mathcal{H}$, is given by

$$\mathcal{H} = \frac{(\gamma_2-1)(\gamma_2+1)q}{2\gamma_1 R_1 T_1}. \tag{3.16}$$

The jump conditions are then given by

$$\frac{P_{CJ}}{P_1} = \frac{\gamma_1 M_{CJ}^2 + 1}{\gamma_2 + 1} \tag{3.17}$$

$$\frac{\rho_{CJ}}{\rho_1} = \frac{\gamma_1(\gamma_2+1)M_{CJ}^2}{\gamma_2(1+\gamma_1 M_{CJ}^2)} \tag{3.18}$$

$$\frac{T_{CJ}}{T_1} = \frac{P_{CJ}}{P_1}\frac{R_1\rho_1}{R_2\rho_{CJ}}. \tag{3.19}$$

3.2.2 Equilibrium Model

The equilibrium CJ model is similar to the 2-γ model that allows different values of the molecular weights and specific heat capacities on either side of the detonation wave. However, in the equilibrium model, the values of the molecular weight and specific heat capacities is not set beforehand but is now a function of the mixture properties. The following analysis may be found in greater detail in [73].

For the equilibrium model, the energy equation give above, Eq. 3.12, must be modified since the assumption of a thermally perfect is no longer valid. The energy equation across the detonation wave now becomes

$$h_1 + \frac{u_1^2}{2} = h_2 + \frac{u_2^2}{2} \tag{3.20}$$

where h is the enthalpy given by

$$h = \sum_{i=1}^{K} Y_i h_i(T). \tag{3.21}$$

The enthalpy of a mixture consisting of K species is the sum of the mass fractions, Y_i, multiplied by their individual values of enthalphy, h_i. Note that the equilibrium model is assumed to be a thermally perfect gas where the enthalpy is only a function of the temperature. The species enthalpies are given by

$$h_i = \int_{T_{ref}}^{T} c_{P_i}(T) dT + \Delta_f h_{i,ref} \tag{3.22}$$

where $\Delta_f h_{i,ref}$ is the heat of formation for species, i, at a reference state of $T_{ref} = 298.15$ K and $P_{ref} = 1$ bar. The values of c_{P_i} are generally given in a polynomial form that has been fitted to tabular, experimental data. The specific gas constant is a function of the average molar mass of the mixture given by

$$\overline{W} = \left(\sum_{i=1}^{K} \frac{Y_i}{W_i} \right)^{-1}. \tag{3.23}$$

The composition of the reactants, Y_{i_1} is known; however, the composition of the products, Y_{i_2} is unknown and must be determined. Since this is an equilibrium model, the composition of the products is given by the equilibrium value:

$$Y_{i_2} = Y_{i_2}^{eq}(P_2, T_2). \tag{3.24}$$

Solving for the equilibrium value is found using an iterative technique that solves a system of equations that define chemical equilibrium. In this work, the equilibrium solution is provided by the Cantera package [74].

The Rayleigh line is still given by Eq. 3.13 since it is only a combination of the mass and momentum equations which have not changed. Since the energy equation for the equilibrium model is different, the equation for the Hugoniot is now given by

$$h_2 - h_1 = (P_2 - P_1)\frac{(\nu_2 + \nu_1)}{2}. \tag{3.25}$$

At the tangency point, the flow velocity behind the wave is sonic and equal to the equilibrium sound sound speed. Guessing the properties at state 2 as well as requiring the velocity to be equal to the sound speed defines an iterative system that may be solved to determine the detonation velocity and properties.

3.3   Injector Modeling

Currently, there is no mass flow injection boundary condition for 2D MOC in the literature. Therefore, a new boundary condition suitable for MOC must be developed. A set of jump equations based on a flow undergoing a sudden expansion is developed here to provide an analytical set of equations to solve along with the MOC compatibility relations in order to provide a mass flow injection boundary condition. This section is concerned with the development of the jump relations and a later section deals with solving these equations in conjunction with the MOC compatibility relations.

Figure 3.5 shows a cross section of an idealized RDE annulus where a premixed

inflow of reactants is being driven by a plenum through a slot nozzle that discharges suddenly into an enlarged channel area. Station 1 is located at the throat of the nozzle and station 2 is located in the channel immediately after the nozzle. Station 3 is located downstream of the throat at a point where the flow has become uniform. The distance between stations 2 and 3 is the transition region where the flow goes from highly nonuniform to uniform. The entire process is assumed adiabatic and the flow is assumed to be isentropic between the plenum and station 1, since the majority of the losses occur during the sudden expansion and transition. Given P_0, T_0, A_1, A_3, and P_3, all other parameters of the system may be determined. The first step in solving this problem is to apply conservation of mass, momentum, and energy for a steady, quasi one-dimensional, inviscid flow between stations 2 and 3. The conservation equations are then given as

$$\rho_1 v_1 A_1 = \rho_3 v_3 A_3 \tag{3.26}$$

$$-\rho_1 v_1^2 A_1 + \rho_3 v_3^2 A_3 = P_1 A_1 + P_2 A_2 - P_3 A_3 \tag{3.27}$$

$$\frac{\gamma}{\gamma - 1}\frac{P_1}{\rho_1} + \frac{v_1^2}{2} = \frac{\gamma}{\gamma - 1}\frac{P_3}{\rho_3} + \frac{v_3^2}{2} = \frac{\gamma}{\gamma - 1}\frac{P_0}{\rho_0}. \tag{3.28}$$

The mass flow rate into the control volume is given by

$$\dot{m} = \frac{A_1 P_0}{\sqrt{T_0}}\sqrt{\frac{\gamma}{R}}M_1\left(1 + \frac{\gamma - 1}{2}M_1^2\right)^{-(\gamma+1)/(2(\gamma-1))} \tag{3.29}$$

where $0 \leq M_1 \leq 1$. If $\dot{m}$ is known, v_3 may be calculated by rewriting the energy equation as a quadratic equation in v_3:

$$\frac{1}{2}v_3^2 + \frac{\gamma}{\gamma - 1}\frac{P_3 A_3}{\dot{m}}v_3 - \frac{\gamma}{\gamma - 1}\frac{P_0}{\rho_0} = 0. \tag{3.30}$$
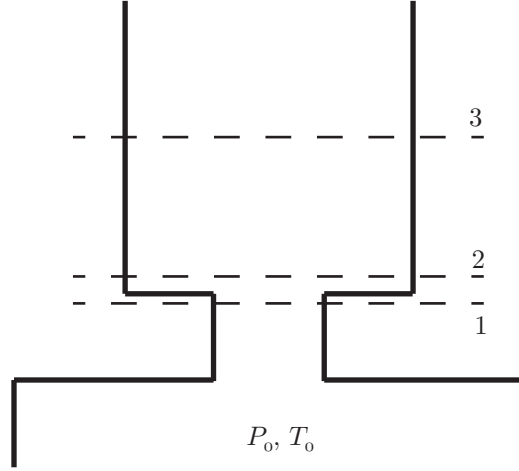
Figure 3.5: Cross-sectional slice of an RDE annulus.

Once v_3 is known, P_2 may be solved for from the momentum equation as

$$P_2 = \frac{\dot{m}(v_3 - v_1) - P_1 A_1 + P_3 A_3}{A_3 - A_1}.$$ (3.31)

Note that Eq. 3.31 is derived by assuming that $A_2 = A_3 - A_1$. This implies the RDE is being fed by a constant area slot injector along the bottom of the annulus. Also note that since the flow in the nozzle before the sudden expansion is isentropic, P_1 may be calculated using the isentropic flow relation.

The solution process for determining the correct $\dot{m}$ and v_3 is to first assume that the flow is choked ($M_1=1$). The next step is to use the isentropic relations to calculate P_1 and then use Eqs. 3.29, 3.30, and 3.31 to calculate $\dot{m}$, v_3, and P_2. If P_2 is less than P_1, the flow is choked and no further calculations are required. When $P_2 > P_1$, the flow is unchoked and an iterative process is required to determine the correct M_1 to match P_1 and P_2. Assuming the transition occurs instantaneously and that the distance between stations 2 and 3 is negligible, the previously derived equations become a set of jump equations analytically describing the injection of
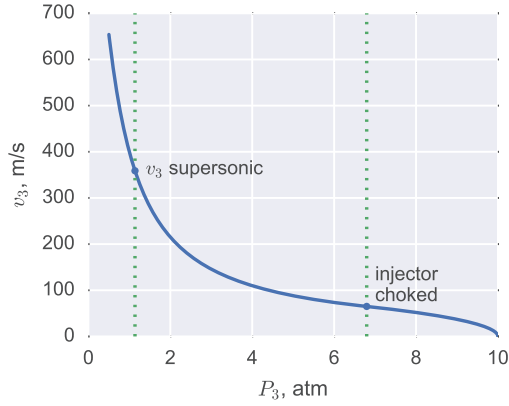
Figure 3.6: v_3 vs. P_3.
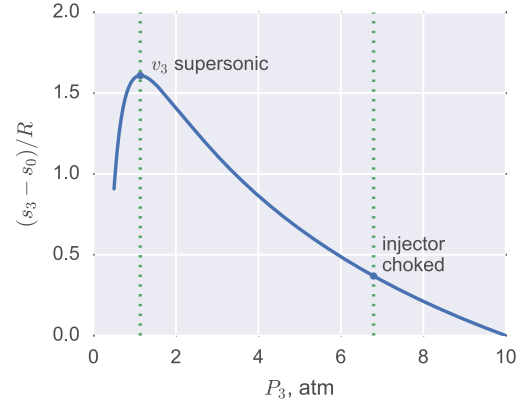
Figure 3.7: $(s_3 - s_1)/R$ vs. P_3.

reactants into an RDE annulus.

The variation in the velocity at station 3 and the change in entropy is examined for a test case in Figs. 3.6 and 3.7. The conditions for the test case are an unburnt stoichiometric hydrogen-air mixture with P_0=10 atm, T_0=300 K, and A_1/A_3=0.2. As the pressure at station 3 is lowered, the flow in the nozzle will eventually choke. If it is lowered even further, the flow in station 3 becomes supersonic. It is important to note that the entropy varies as P_3 changes. This entropy gradient requires that the rotational method of characteristics be used to model the inflow correctly.

Chapter 4: Method of Characteristics Modeling

The steady, two-dimensional, isentropic method of characteristics is used to numerically simulate the flowfield for a stably operating RDE. A predictor-corrector method is used to evaluate the compatibility relations along the characteristics. The algorithms used to perform the unit processes are based on those given in [75], but due to large entropy gradients generated by the inflow unit process, a modification in how the streamline properties are calculated is required.

4.1 Characteristic Equations and Compatibility Relations

The Euler equations for steady, two-dimensional, isentropic flow are given by:

$$\rho\frac{\partial u}{\partial x} + \rho\frac{\partial v}{\partial y} + u\frac{\partial \rho}{\partial x} + v\frac{\partial \rho}{\partial y} = 0 \tag{4.1}$$

$$\rho u\frac{\partial u}{\partial x} + \rho v\frac{\partial u}{\partial y} + \frac{\partial P}{\partial x} = 0 \tag{4.2}$$

$$\rho u\frac{\partial v}{\partial x} + \rho v\frac{\partial v}{\partial y} + \frac{\partial P}{\partial y} = 0 \tag{4.3}$$

$$u\frac{\partial P}{\partial x} + v\frac{\partial P}{\partial y} - a^2 u\frac{\partial \rho}{\partial x} - a^2 v\frac{\partial \rho}{\partial y} = 0 \tag{4.4}$$

There are four characteristics present in these equations. They are the left running Mach line, the right running Mach line, and the streamline which is a repeated

characteristic. The characteristic equations are given by:

$$\lambda_{\pm} = \tan(\theta \pm \alpha) \text{ (eq. for the Mach lines)} \tag{4.5}$$

$$\lambda_o = \frac{v}{u} \text{ (eq. for the streamline)} \tag{4.6}$$

The compatibility equation that must be satisfied along the left and right Mach lines is given by

$$\frac{\sqrt{M^2 - 1}}{\rho V^2} dP_{\pm} \pm d\theta_{\pm} = 0. \tag{4.7}$$

The compatibility equations along a streamline are given by

$$dP - a^2 d\rho = 0 \tag{4.8}$$

$$\rho V dV + dP = 0. \tag{4.9}$$

Note that the last equation is the differential form of Bernoulli's equation. For a perfect gas, a closed form solution is available. Combining Eqs. 4.8 and 4.9 with the differential form of the ideal gas law,

$$\frac{dP}{P} = \frac{d\rho}{\rho} + \frac{dT}{T} \tag{4.10}$$

yields

$$dT = -\frac{\gamma - 1}{2\gamma R} V^2. \tag{4.11}$$

Integrating this equation from T_0 to T and from 0 to V and substituting in the definition of the Mach number, $M = V/a$, gives

$$\frac{T_0}{T} = 1 + \frac{\gamma - 1}{2} M^2, \tag{4.12}$$

which is the definition of the stagnation temperature. Combining this with the isentropic relations,

$$\frac{P_0}{P} = \left(\frac{\rho_0}{\rho}\right)^{\gamma} = \left(\frac{T_0}{T}\right)^{\gamma/(\gamma - 1)}, \tag{4.13}$$

gives

$$\frac{P_0}{P} = \left(1 + \frac{\gamma - 1}{2} M^2\right)^{\gamma/(\gamma-1)} \tag{4.14}$$

$$\frac{\rho_0}{\rho} = \left(1 + \frac{\gamma - 1}{2} M^2\right)^{1/(\gamma-1)} \tag{4.15}$$

$$\tag{4.16}$$

which are the definitions of the stagnation pressure and stagnation density. There-fore, instead of numerically solving Eqs. 4.8 and 4.9, the values of the stagnation pressure and density along a streamline are used.

4.2   Mass-Stagnation Method

The mass-stagnation method is an extension of the mass-entropy method cre-ated by Powers and O'Neill [76] for the case when the freestream conditions ahead of an oblique shock are not constant. The mass-entropy method was created to ad-dress the large increase in errors associated with flows with strong entropy gradients. Most MOC unit processes (for example, see [75]), assume a linear entropy gradient. For very strong entropy gradients, this assumption may lead to large errors in the conservation quantities. One way to address this problem is to track the value of the mass integral along with the entropy (or stagnation values in the mass-stagnation method). This approach is successful since the gradient of the mass integral is much smaller than the gradient of the entropy or stagnation values.

The mass-stagnation method is based on tracking the mass integral defined by a stream function for compressible, two-dimensional flow. The continuity equation

37

for compressible, two-dimensional flow is

$$\frac{\partial}{\partial x}\rho u + \frac{\partial}{\partial y}\rho v = 0. \tag{4.17}$$

A stream function, ψ, that satisfies this equation has the properties

$$\rho u = \frac{\partial \psi}{\partial y} \tag{4.18}$$

$$\rho v = -\frac{\partial \psi}{\partial x}. \tag{4.19}$$

It can be shown that lines of constant ψ occur along streamlines and that the difference in the value of ψ between two streamlines represents the integral of the mass flow through those streamlines. This integral may be computed as

$$\psi_2 - \psi_1 = \int_{(x_1,y_1)}^{(x_2,y_2)} (\rho u dy - \rho v dx). \tag{4.20}$$

This integral is solved for ψ_2 using the trapezoidal rule:

$$\psi_2 = \psi_1 - (x_2 - x_1)\left(\frac{\rho_1 v_1 + \rho_2 v_2}{2}\right) + (y_2 - y_1)\left(\frac{\rho_1 u_1 + \rho_2 u_2}{2}\right). \tag{4.21}$$

The mass-stagnation method requires that the value of the mass integral, the stagnation pressure, and the stagnation temperature are stored in a look-up table along either the inflow, detonation, or oblique shock boundary. Once the look-up table is created, the stagnation values along a streamline are found by calculating the value of ψ for that streamline and linearly interpolating for the correct value of the stagnation pressure and density.

In practice, determining the streamline is only required for the interior point unit processes shown in Fig. 4.1. Normally, the steamline is found by interpolating

38
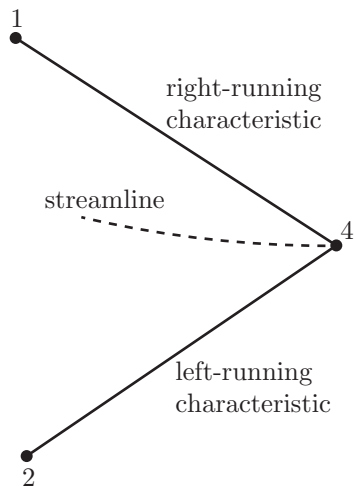
Figure 4.1: Illustration of interior-point unit process.

between points 1 and 2. Using the mass-stagnation method, the streamline proper-

ties are found by iteratively determining the the value of the mass integral at point

4, ψ_4. Following Eq. 4.21, there are two choices for calculating ψ_4. These are

$$\psi_4 = \psi_1 + (x_1 - x_4)\left(\frac{\rho_1 v_1 + \rho_4 v_4}{2}\right) - (y_1 - y_4)\left(\frac{\rho_1 u_1 + \rho_4 u_4}{2}\right) \tag{4.22}$$

$$\psi_4 = \psi_2 + (x_2 - x_4)\left(\frac{\rho_2 v_2 + \rho_4 v_4}{2}\right) - (y_2 - y_4)\left(\frac{\rho_2 u_2 + \rho_4 u_4}{2}\right) \tag{4.23}$$

depending on whether the integration occurs between points 1 and 4 and 2 and

4, respectively. The current implementation calculates the integral both ways and

takes the average. More detail on the implementation of the interior point unit

process may be found in Appendix A.

4.3   Mass Injection Boundary Condition

The jump equations for a flow undergoing a sudden expansion developed pre-

viously (see Eqs. 3.29, 3.30, and 3.31) are used in the creation of an inflow unit

process to create a new boundary condition to simulate mass injection. Figure 4.2
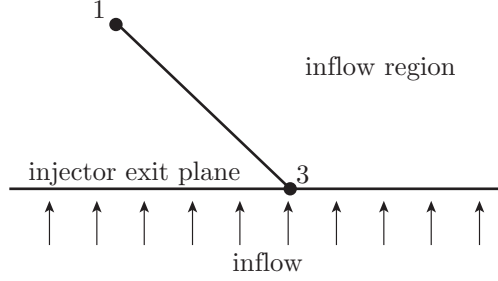
Figure 4.2: Illustration of a inflow point unit process.

illustrates the unit process along the injector boundary.

Solving for points along the inflow boundary is similar to solving for points along an oblique shock. Instead of iterating for the correct pressure and shock properties using the oblique shock relations, the pressure and inflow properties are found iteratively using Eqs. 3.29, 3.30, and 3.31 for flow undergoing a sudden expansion. Note that if P_3 is too high, the inflow is blocked and the boundary is treated as a solid wall instead. If $P_3 < P_0$, the inflow calculation is performed and the flow may be either unchoked or choked depending upon the value of P_3 and P_0. It is important to note that the sudden expansion jump relations are derived in the laboratory reference frame. For a given value of P_3, v_3 is calculated, and then the velocity of the reference frame, $u_3 = u_{lab}$, is added, giving $V_3 = \sqrt{v_3^2 + u_3^2}$ and $\theta_3 = \tan(v_3/u_3)$. The goal is to then find P_3 and θ_3 that satisfies the sudden expansion jump equations and MOC compatibility relations. It should also be noted that this boundary condition is similar to the boundary condition developed by Paxson and Wilson [77]. Their boundary condition was developed for a traditional CFD solver and may be thought of as the finite volume equivalent of the inflow boundary condition developed in this work.

4.4 Slip Line Boundary Condition

In an RDE, slip lines form along the boundaries between the inflow, detonation products, and the detonation products of the previous wave that have been processed through an oblique shock. This unit process is not commonly given in the literature or in textbooks, although there is an overview of a slip-line process for irrotational flow in Thompson [78]. The unit process for rotational flow is given here due to its importance for the RDE model being developed.
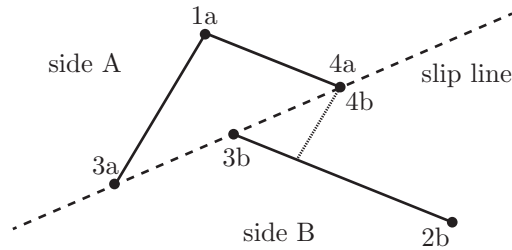
Figure 4.3: Illustration of a slip point unit process.

Figure 4.3 illustrates the unit process for a new point along a slip line. The goal is to determine the state at point 4 on side A. Along a slip line, the pressure and flow angle must match. This leads to an iterative process to match the pressure and flow angle. The system is set up by first solving for point 4a using a prescribed-pressure unit process. This is similar to the free-pressure unit process outlined by Zucrow and Hoffman, but now the pressure along the boundary does not have to be constant (i.e., P_{4a} does not have to be equal to P_{3a} or P_{3b}). Once this is done, the location and flow angle of point 4a is known. Point 4b is now calculated using the indirect wall point unit process given by Zucrow and Hoffman [75]. This gives a value of the pressure at point 4b. A residual can now be defined as the difference in

41

the prescribed pressure given for point 4a and the calculated pressure at point 4b. An iterative solver is then used to determine the correct pressure that matches the pressure and flow angle.

4.5   Interpolating within the Characteristic Mesh

To initialize a new solution from a previous solution, an interpolation method is required to find the flow properties at points within the characteristic mesh. The interpolation process for a point inside a cell created by an interior point unit process is shown in Fig. 4.4. A nonlinear solver iterates on the correct locations of points $1'$ and $2'$ that give the desired point, $4'$. Point $1'$ is found by interpolating between points 1 and 3 and point $2'$ is found by interpolating between points 2 and 3. The interpolation process for cells along slip lines, the inflow boundary, and the shock boundary are similar to the interior cell method.
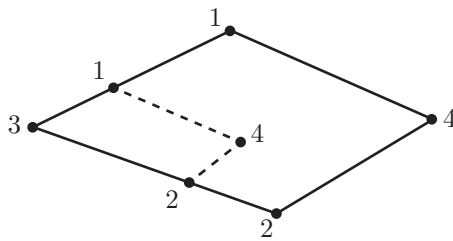
Figure 4.4: Illustration of interpolating within an interior flow cell.

When performing a shock-point unit process that is using information from a previous solution, the interpolation methods are called to determine the properties just ahead of the shock. This shock-point unit process is similar to that outlined in Zucrow and Hoffman but the properties just ahead of the shock must also be iterated on.

Lastly, the interpolation methods are also called to determine the properties ahead of the detonation wave in the inflow region. Once the properties are found, they are averaged to get pressure, temperature, and flow angle. The pressure and temperature are used to determine the detonation velocity and jump conditions. The flow angle determines the inclination of the detonation. The point at the top of the detonation wave on the post-detonation side becomes point i_1, and the detonation-oblique shock interaction is performed and a new RDE solution is initialized.

Chapter 5: Reduced Order Model of an RDE

5.1 Overview of Marching Algorithm

There are three distinct regions in the RDE model being developed, as shown in Fig. 5.1. There is the post-oblique shock region, post-detonation region, and inflow region. The MOC solutions in these regions are marched out concurrently. Communication between the regions is handled by the slip line unit process. How these regions are initialized and marched out is described in more detail in the following sections.
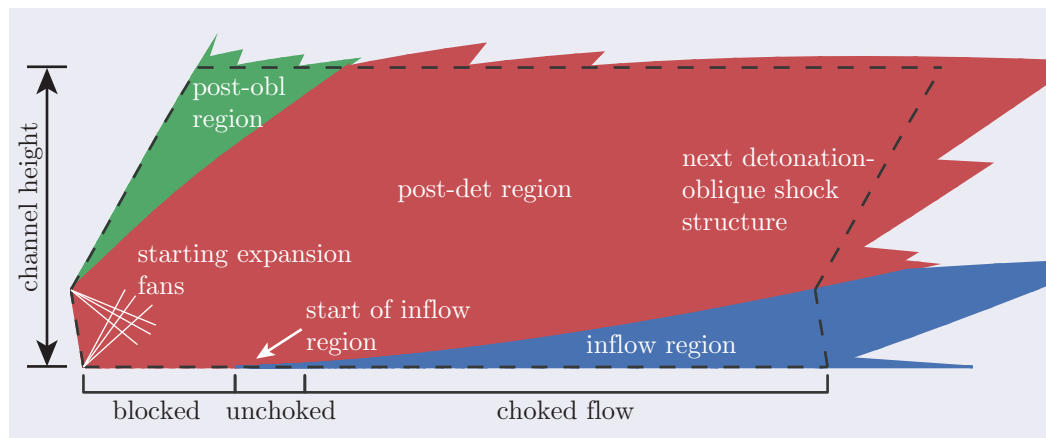
Figure 5.1: MOC solution ($h = 17.7$ cm, $l = 43.98$ cm, $w = 1$ cm, $A_1/A_3 = 0.3$, $P_0 = 10$ atm, and $T_0 = 300$ K).

The dashed lines in Fig. 5.1 represent the domain of the RDE. On the left side, the domain starts along the detonation wave and oblique shock. The top line

represents the RDE exit. For one wave operation, the distance between the left detonation and oblique shock and the right (next) detonation and oblique shock is equal to the average circumference of the RDE. Note that parts of the solution have marched out past these dotted lines. Since MOC is a marching process, the characteristics are marched out along points where the right and left characteristics cross. These points are not defined beforehand so to ensure that the solution covers the entire RDE domain, the solution is marched until the top and right lines are completely covered by the characteristic mesh. The previously described interpolation methodology is then used to calculate points along the top and right domain boundaries.

Lastly, along the bottom boundary, the pressure from the detonation wave is higher than the plenum pressure of the injection system. The model treats this boundary as a solid wall implying that the flow from the injector is blocked. Once the pressure decreases, reactants start to flow into the domain and the flow in the injector is unchoked. As the pressure continues to decrease, the flow becomes choked and remains that way until the next detonation wave. These blocked, unchoked, and choked sections of the bottom boundary are marked on Fig. 5.1 to illustrate where they occur.

5.1.1   Post-Detonation Region

The post-detonation region is initialized using the centered expansion fans at the top and bottom of the detonation wave shown in Fig. 5.1. Resolution in
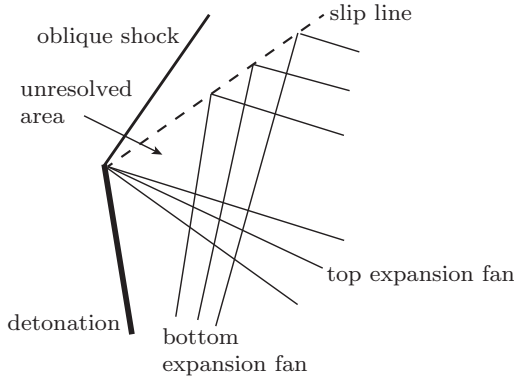
Figure 5.2: Unresolved area in post-detonation region.
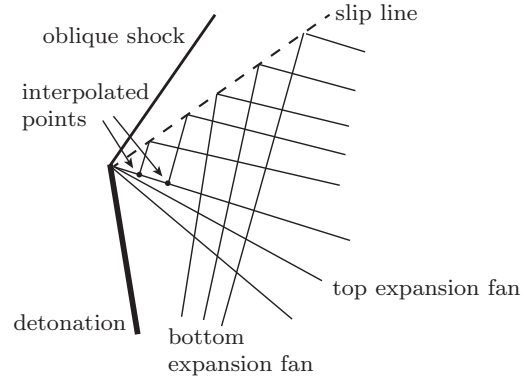
Figure 5.3: Fix to increase resolution in the post-detonation region.

this region is set by choosing the number of characteristics in the top and bottom expansion fans. Since the flow behind the detonation is sonic, the first characteristic in the expansion fans is calculated for a Mach number slightly greater than one as described in [79] when initializing a nozzle flow calculation.

If just the top and bottom expansion fans are used to generate the characteristic mesh in the post-detonation region, a small region where the oblique shock, slip line, and detonation intersect may suffer from a lack of resolution. This is shown in Fig. 5.2. To increase the resolution in this area, additional points are interpolated along the last characteristic of the top expansion fan. Left-running characteristics from these points intersect the slip line and increase resolution in the area around the detonation-oblique shock interaction point.

In the post-detonation region, the lookup tables for the mass-stagnation method are generated along the detonation boundary. The lookup tables are initialized using a point representing the bottom of the detonation and another point representing the top so there are only two points in the lookup tables. Since the detonation is

assumed planar, the flow state is constant just behind the detonation wave. There-fore, the values of the stagnation pressure and density along the streamlines are the same for every streamline. Any value of ψ in the post-detonation region should just return the stagnation pressure and density calculated behind the CJ detonation. It should be noted that this means the flow in the post-detonation region is irrotational which is not an issue for the rotational method of characteristics.

The top boundary of the post-detonation region is defined by a slip line bor-dering the post-oblique shock region. Along the bottom boundary, the boundary is treated like a solid wall as shown in Fig. 5.1 until the pressure along the bottom has decreased below the plenum pressure. Once this occurs, the inflow region is initialized and the boundary becomes a slip line bordering the inflow region. The details of initializing the inflow region are given in the next section.

5.1.2   Inflow Region

The inflow region is initialized when the pressure along the bottom boundary decreases below the plenum pressure in the injection system as shown in Fig. 5.4. This occurs when the wall point calculations from reflected right-running character-istics in the post-detonation region show that the pressure is less than the plenum pressure. Once the pressure calculated from a wall point unit process shows a pressure less than the plenum pressure, an inflow point calculation is performed to determine the start of the inflow region and the initial angle of the slip line separat-ing the post-detonation and inflow regions. This point is labeled point 1 in Fig. 5.4.

Figure 5.4: Initialization of the inflow region.

Once the inflow region has been initialized, the first right-running characteristic in the post-detonation region that reflects off the slip line is used to generate the initial value line in the inflow region. The reflection point along the slip line where this occurs is labeled point 2 in Fig. 5.4. The initial value line is the right-running characteristic from the slip line in the inflow region that hits the injector boundary at point 3.

Recalling the slip line unit process depicted in Fig. 4.3, a left running characteristic is required from the inflow region to perform the slip point unit process at point 2. This left running characteristic is generated at a point that is interpolated between points 1 and 3 along the inflow boundary. Since point 3 is not known when point 2 needs to be calculated, a guess is made that the state at point 3 is equal to the state at point 1. Once point 2 is calculated, point 3 is calculated using the inflow point unit process described in Chapter 4. Point 2 is then recalculated using the updated value at point 3 to interpolate for the left running characteristic to perform the slip line unit process. This iterative process is repeated until the values at point 2 and 3 no longer change within a specified tolerance. A similar process

occurs when initializing external hypersonic flows with curved leading edges [75].

Once the right running characteristic between points 2 and 3 is created, the characteristic is used as an initial value line to start marching out the inflow region. Resolution in the inflow region is controlled by specifying the number of points along the 2-3 line to start left running characteristics off of. Note that the flow properties at these points are interpolated between points 2 and 3.

The lookup tables for the mass-stagnation method are generated along the inflow boundary. At each point, ψ, P_0, and ρ_0 are calculated and stored so that streamline information may be determined in the interior of the region.

5.1.3 Post-Oblique Shock Region

The post-oblique shock region is initialized using the calculated oblique shock and slip line angles from solving the analytical system described in Chapter 3 and the first left running characteristic from the post-detonation region to reflect off the slip line. An illustration of the initialization procedure is shown in Fig. 5.5. The procedure for calculating points 2 and 3 is similar to the procedure for initializing the inflow region. To calculate point 2 on the slip line, a point is interpolated between points 1 and 3. The properties at point 3 is initially assumed to be equal to the properties at point 1. After point 2 is calculated, the left running characteristic intersects the shock and a shock point unit process is performed. Point 2 is then calculated again with the new values at point 3. This process is repeated until the properties at points 2 and 3 change less than some prescribed error tolerance.
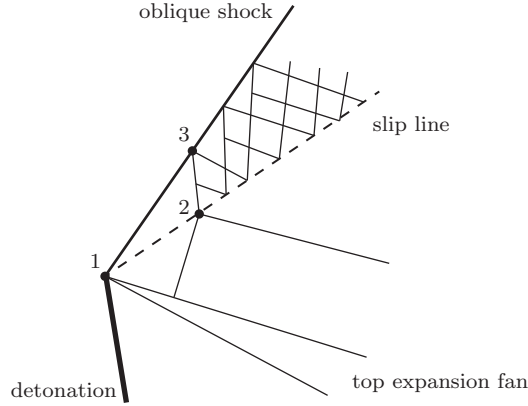
Figure 5.5: Initialization of the post-oblique shock region.

Similar to the inflow region, resolution is controlled by specifying the number of points along the initial value line created between points 2 and 3. It is also important to note that the marching algorithm for the post-oblique shock region is different than the one used in the post-detonation and inflow regions. In Fig. 5.5, an additional point is created along the left running characteristics that intersect the shock. This is done to increase resolution and this marching method is commonly seen in solving external hypersonic flowfields [75].

Lastly, the lookup tables for the post-oblique shock region are generated along the oblique shock. Once a point on the oblique shock is created, the lookup tables are updated with the values of ψ, P_0, and ρ_0 at the point.

5.2   Averaging Ahead of the Detonation

Performing the CJ detonation calculation requires that the pressure and temperature ahead of the wave are known. The flow angle is also required to determine the inclination of the detonation wave. Lastly, the flow velocity is required so a

reference frame velocity may be chosen that ensures the flowfield is steady. Since the current model shown in Fig. 3.2 assumes a planar wave, averaged values are used to represent the varying conditions ahead of the detonation wave.
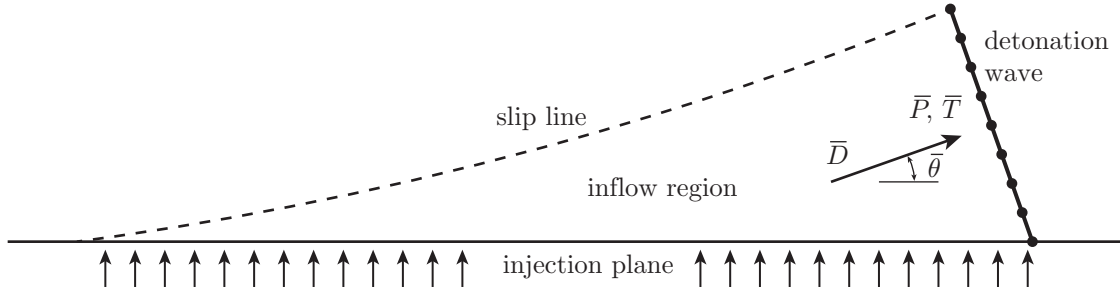
Figure 5.6: Illustration of the inflow region.

The method of averaging chosen in this work is an extension of a type of averaging known as flux averaging or mixed out averaging [80]. This is done to ensure that mass, momentum, and energy are conserved across the detonation wave. In front of the detonation wave shown in Fig. 5.6, there exist gradients of velocity, flow angle, pressure, and temperature. The planar detonation assumption along with determining the detonation inclination and reference frame velocity require averaged values of u, v, P, and ρ. Across the wave, there are five fluxes going into the wave that should be conserved. These are the mass, x-momentum, y-momentum, energy, and entropy fluxes. Since there are only four averaged variables to represent the state, only four of the fluxes can be satisfied exactly. In flux averaging, the mass, momentum, and energy fluxes are satisfied and the entropy of the averaged flow is increased over its actual value. Physically, flux averaging is the equivalent of sending a nonuniform flow down a long friction-less tube until the flow has become uniform. The increase in entropy associated with this process may be thought of as

the entropy of mixing.

To calculate the flux averaged values, points along the detonation wave are interpolated to provide profiles of u, v, P, and ρ that can be integrated. The four fluxes are then defined as

$$\mathcal{M} = \rho(un_x + vn_y) \tag{5.1}$$

$$\mathcal{P}_x = \rho(u^2 n_x + uvn_y) + pn_x \tag{5.2}$$

$$\mathcal{P}_y = \rho(uvn_x + v^2 n_y) + pn_y \tag{5.3}$$

$$\mathcal{H} = \left[\rho \left(e + \frac{V^2}{2} \right) + p \right] (un_x + vn_y) \tag{5.4}$$

which represent the mass, x-momentum, y-momentum, and energy fluxes, respectively. The averages of these fluxes are given by integrating along the detonation and dividing by the area ahead of the detonation wave. These averages are defined as

$$\overline{\mathcal{M}} = \frac{1}{A} \int \mathcal{M} dA \tag{5.5}$$

$$\overline{\mathcal{P}_x} = \frac{1}{A} \int \mathcal{P}_x dA \tag{5.6}$$

$$\overline{\mathcal{P}_y} = \frac{1}{A} \int \mathcal{P}_y dA \tag{5.7}$$

$$\overline{\mathcal{H}} = \frac{1}{A} \int \mathcal{H} dA. \tag{5.8}$$

There are now four unknowns, $\overline{u}$, $\overline{v}$, $\overline{P}$, and $\overline{\rho}$ in four equations, Eqs. 5.1, 5.2, 5.3, and 5.4. A nonlinear equation solver may now be used to determine the averages of the primitive variables that will exactly recover the mass, momentum and energy fluxes. Unfortunately, there is an entropy increase associated with this type of averaging but any averaging method loses some information in the process. An analysis

52

of the entropy increase due to the flux averaging shows that it is approximately 0.5% of the entropy increase due to the detonation wave and approximately 7.5% of the entropy increase due to the injection process. Therefore, the increase in entropy due to flux averaging does not significantly effect the overall entropy generation in an RDE.

With $\overline{P}$ and $\overline{\rho}$ known, a CJ detonation calculation is performed. The detonation inclination is given by $\overline{\theta} = \tan^{-1}(\overline{v}/\overline{u})$. Note that the detonation inclination determines the line along which points are interpolated, therefore, an iterative process is required to find the detonation inclination that matches the angle of the line points are interpolated on. Lastly, the average velocity ahead of the wave, $\overline{V} = \sqrt{\overline{u}^2 + \overline{v}^2}$, should be equal to the detonation velocity, D, if the steady-state approximation is to hold. This process is explained in the next section.

5.3   Counter-flow and Reference Frame Velocity

In the laboratory frame of reference, the reactants ahead of the detonation wave have a non-zero component of velocity in the azimuthal direction due to expansion waves generated by the previous detonation. This velocity component is defined as the counter-flow since it works to decrease the observed detonation speed in the laboratory frame. Note that this is not to be confused with the backflow which is defined as the flow of detonation products into the injection system caused by the high pressures generated by the passing detonation wave. The MOC model developed here is able to handle counter-flow encountered by the detonation with

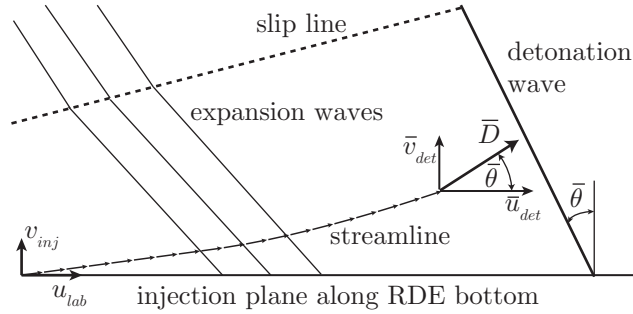respect to the average properties ahead of the detonation.

Figure 5.7: A zoomed in view of the flow ahead of a detonation in an RDE in the wave-fixed reference frame.

Figure 5.7 gives a zoomed in view of the flow ahead of the detonation in the wave-fixed reference frame. A streamline is shown that starts at the injection plane and ends at a point just before the detonation wave. At the injection plane, there is a vertical component of the velocity, v_{inj}, determined by the inflow boundary condition previously described. The horizontal component of the velocity, u_{lab}, is the velocity of the injection plane with respect to an observer situated on the detonation wave. As a particle travels along this streamline, expansion waves from the previous detonation accelerate the particle in the both the axial and azimuthal directions. By the time the particle reaches the detonation wave, it must have a total velocity equal to the detonation velocity, D, to satisfy the steady-state requirement of the model being developed. The value of the counter-flow is equal to $u_{det} - u_{lab}$ and is the horizontal component of the velocity ahead of the detonation wave in the laboratory frame that effectively decreases the observed detonation velocity.

It is important to note that since this model assumes a planar detonation wave, the streamlines ahead of the detonation wave are mass averaged to get the flow
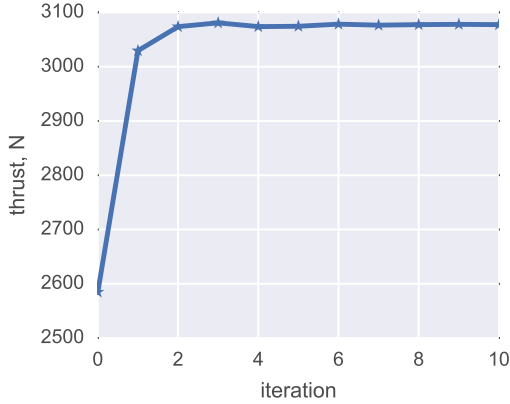
Figure 5.8: Convergence of the thrust as the MOC solution is iterated on (h = 17.7 cm, l = 43.98 cm, w = 1 cm, A_1/A_3 = 0.3, P_0 = 10 atm, and T_0 = 300 K).
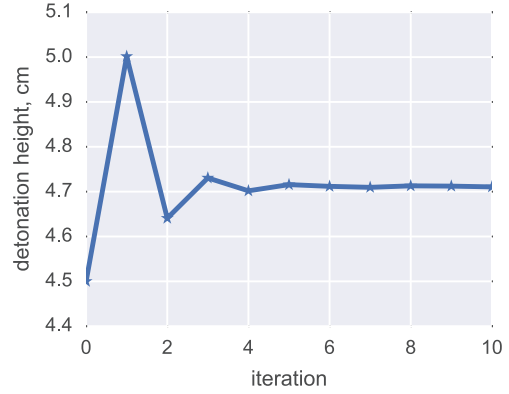
Figure 5.9: Convergence of the detonation height as the MOC solution is iterated on (h = 17.7 cm, l = 43.98 cm, w = 1 cm, A_1/A_3 = 0.3, P_0 = 10 atm, and T_0 = 300 K).

velocity, flow angle, pressure, and temperature ahead of the wave. This information is used to perform a CJ detonation calculation to determine the detonation velocity, D. The value of u_{lab} is adjusted so that $u_{det}^2 + v_{det}^2 = D^2$. The process of adjusting u_{lab} to get the correct steady-state solution is given in the next section.

5.4 Solution Procedure

The following procedure uses the previously developed tools to generate the MOC solution shown in Fig. 5.1:

1. The first step is to provide initial guesses for the pressure and temperature ahead of the detonation wave, the detonation inclination angle, and the detonation height. A first guess for the laboratory reference frame is to assume no counter-flow (i.e., $u_{lab} = D\cos(\theta)$). The conditions ahead of the oblique shock wave are assumed constant and equal to the conditions at i_1 in Fig. 3.2. The

properties at this state are found by assuming an isentropic expansion of the detonation products.

2. Calculate the detonation-oblique shock interaction and begin marching out the post-oblique shock, post-detonation, and inflow regions until the stopping condition is met.

3. Interpolate for the pressure, temperature, and flow angle ahead of the detonation wave. Where the detonation intersects the slip line is the new detonation height. This may be seen in Fig. 5.1 where the dashed line in the inflow region intersects the boundary between the inflow and post-detonation regions. The intersection point on the post-detonation side is used for the condition at i_1 to perform the detonation-oblique shock calculation. Note that future shock point unit processes will interpolate for conditions ahead of the oblique shock using data from the previous solution. The reference frame velocity, u_{lab}, is also adjusted so the averaged velocity ahead of the detonation is equal to the detonation velocity given by a CJ solver. Note this also affects the flow angle in front of the detonation.

4. Repeat steps 2 and 3 until the solution converges. This occurs when changes in the pressure, temperature, flow angle, detonation height, and laboratory frame velocity do not change between solutions.

Figures 5.8 and 5.9 show the convergence history of the thrust and detonation height as steps 2 and 3 are repeated. After approximately 5 to 6 iterations, the solution has converged. This was found to be the case for most cases tested.
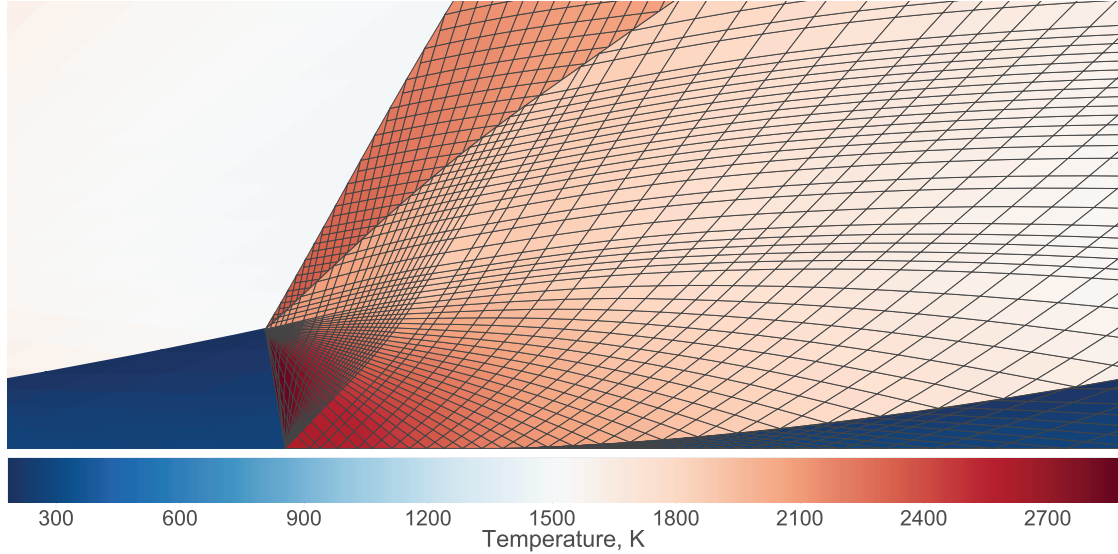
Figure 5.10: Temperature contours of an MOC solution ($h = 17.7$ cm, $l = 43.98$ cm, $w = 1$ cm, $A_1/A_3 = 0.3$, $P_0 = 10$ atm, and $T_0 = 300$ K).

Putting everything together, a contour plot of a MOC solution for the case where $h = 17.7$ cm, $l = 43.98$ cm, $w = 1$ cm, $A_1/A_3 = 0.3$, $P_0 = 10$ atm, and $T_0 = 300$ K for stoichiometric hydrogen-air is given in Fig. 5.10. Qualitatively, this compares very well with the CFD solution in Chapter 2 (Fig. 2.12). The advantage of the MOC method is that the MOC solution took less than 30 seconds on a desktop computer whereas the CFD solution took several hours on a supercomputer. A quantitative comparison of the MOC solution to the CFD solution is given in the next chapter.

Another advantage of the MOC solution over other reduced order models are computed two-dimensional profiles. For example, the MOC solution is capable of calculating inflow and outflow profiles to determine the variation in flow variables such as velocity or pressure. Figure 5.11 shows the axial velocity profile on the
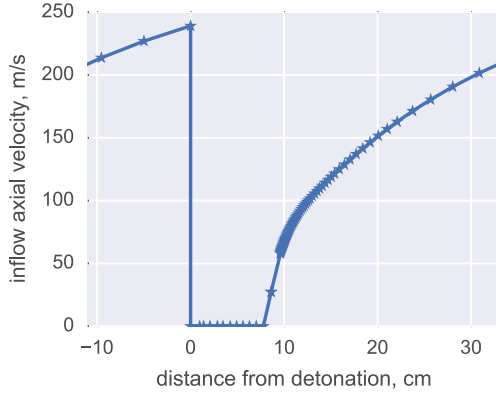
Figure 5.11: Inflow velocity profile (h = 17.7 cm, l = 43.98 cm, w = 1 cm, A_1/A_3 = 0.3, P_0 = 10 atm, and T_0 = 300 K).
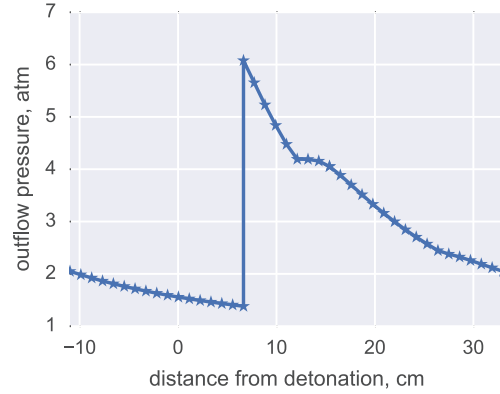
Figure 5.12: Outflow pressure profile (h = 17.7 cm, l = 43.98 cm, w = 1 cm, A_1/A_3 = 0.3, P_0 = 10 atm, and T_0 = 300 K).

inflow plane and Fig. 5.12 shows the pressure profile at the exit of the RDE. Unlike one-dimensional models, the MOC model is able to calculate these profiles.

5.5 Multi-Wave Solutions

Lastly, the MOC model is able to handle multiple waves. This is accomplished by dividing the horizontal length of the domain by the number of waves. The MOC solution is marched out on this smaller domain until a converged solution is found. This solution is then repeated for the number of specified waves to give the final solution. An example of a two wave solution with the characteristic mesh shown behind one of the detonations is shown in Fig. 5.13. Figure 5.14 shows a three wave solution.

Figure 5.13: Temperature contours for a two wave solution ($h = 17.7$ cm, $l = 43.98$ cm, $w = 1$ cm, $A_1/A_3 = 0.3$, $P_0 = 10$ atm, and $T_0 = 300$ K).

Figure 5.14: Temperature contours for a three wave solution ($h = 17.7$ cm, $l = 43.98$ cm, $w = 1$ cm, $A_1/A_3 = 0.3$, $P_0 = 10$ atm, and $T_0 = 300$ K).

Chapter 6:   Analysis of the Reduced Order Model
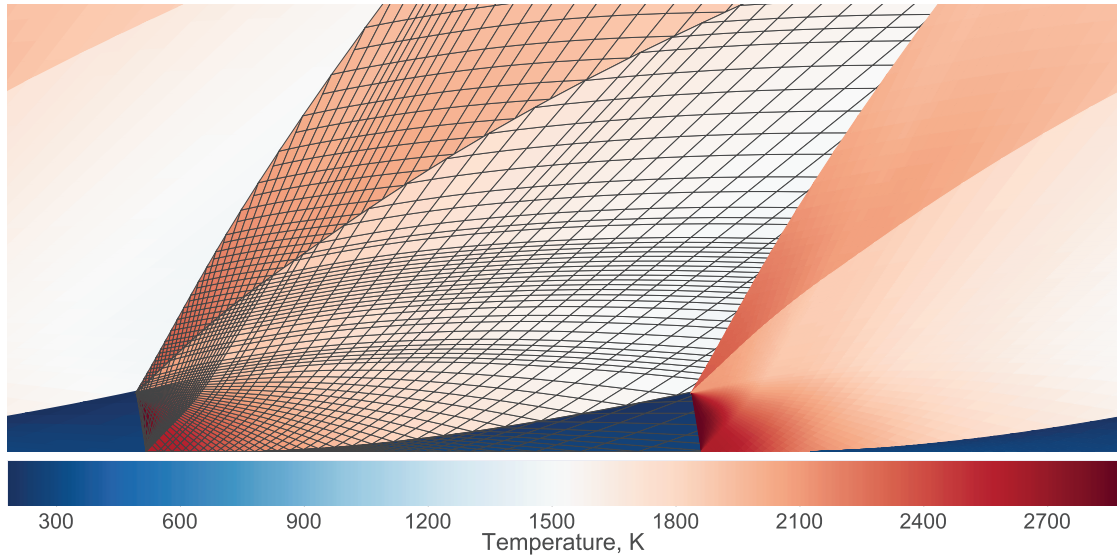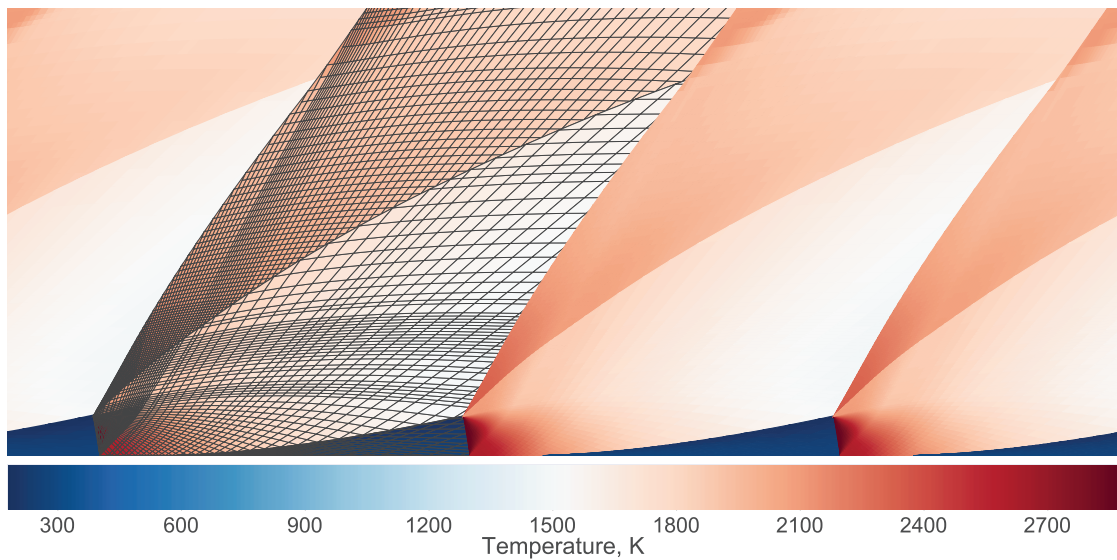
6.1   Comparison to CFD Simulations

The steady state, MOC model developed here is compared to conventional, unsteady CFD simulations that have reached a quasi-steady state solution. Results from Schwer and Kailasanath [15] are reproduced here for comparison. The CFD model of Schwer and Kailasanath solves the unsteady, two-dimensional Euler equations. Chemical reactions are modeled using a single step reaction mechanism along with an induction time parameter model. The solver uses a flux corrected transport algorithm that is commonly used for high-speed reacting flows. It is important to note that since this simulation uses an Euler solver, the deflagration wave is a result of numerical viscosity. Schwer and Kailasanath found that in their simulations, the amount of reactants consumed in the deflagration was approximately 10% [15]. Some experiments have found that up to 20% of reactants may be burned in the deflagration wave [2]. The CFD model is considered to provide a reasonable estimate of the amount of reactants that go through the deflagration instead of the detonation in a premixed RDE.

The MOC solutions presented here use the 2-γ model in [15]. The parameters for this model are $\gamma_1 = 1.40275$, $\bar{M}_1 = 20.9114 \, \text{gm/mol}$, $\gamma_2 = 1.24259$, $\bar{M}_2 = 23.9079$

gm/mol, and $q = 3.48$ MJ/kg. The pre-detonation properties, γ_1 and $\bar{M}_1$, are used in the inflow region. The post-detonation properties, γ_2 and $\bar{M}_2$, are used in the post-detonation and post-oblique shock regions.

Temperature contours in an RDE flowfield are shown in Figs. 5.10, 5.13, and 5.14. The characteristic mesh behind the detonation and oblique shock is also shown. The right boundary is periodic with the rest of the solution continuing on the left side. Qualitatively, this solution looks similar to CFD simulations with the exception of the deflagration wave and Kelvin-Helmholtz instability. Quantitative results comparing various properties for different area ratios are shown in Figs. 6.1, 6.2, 6.3, and 6.4. The specific impulse is calculated as

$$I_{sp} = \frac{F}{g_0 \dot{m}_f} \tag{6.1}$$

where the thrust is given by

$$F = \int_{exit} \left[\rho v^2 + (P - P_{exit}) \right] dA. \tag{6.2}$$

Integration occurs along the top of the RDE exit and the back pressure, P_{exit}, is assumed to be at 1 atmosphere. The fuel flow rate is given by integrating

$$\dot{m}_f = \int_{in} \rho_f v dA \tag{6.3}$$

along the bottom wall where inflow is occurring. These definitions are used in order to match the numerical simulations given in [15].

The model predictions closely match the CFD solution, but it predicts slightly higher performance and fuel flow rates. The model does not match the height of the detonation wave in the axial direction. The higher performance predictions and

61
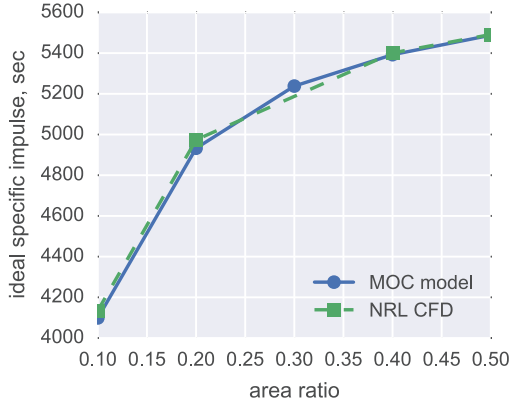
Figure 6.1: I_{sp} vs. A_1/A_3.
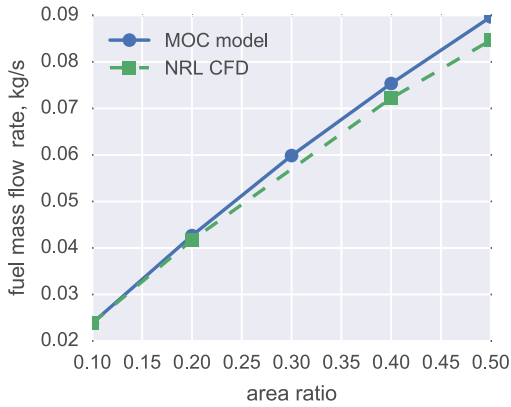
Figure 6.2: F vs. A_1/A_3.

Figure 6.3: $\dot{m}_f$ vs. A_1/A_3.
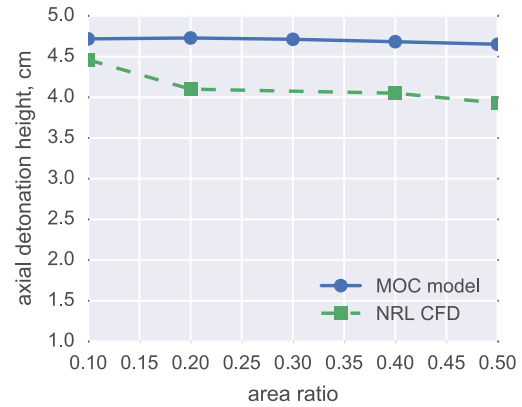
Figure 6.4: h vs. A_1/A_3.

higher detonation heights are most likely due to the absence of a deflagration wave in the model. Instead of reactants being consumed in a low pressure burning process, all of the reactants in the MOC model are burned through a more thermodynamically efficient detonative process.

Solutions for $A_1/A_3 = 0.1$ and 0.5 are shown in Figs. 6.5 and 6.6. The solutions appear qualitatively similar to those of Schwer and Kailasanath [15]. The 0.5 area ratio case starts the inflow process further behind the detonation than the 0.1 case for both the MOC model and the CFD simulations.

Results examining the effect of the height of the RDE annulus on specific
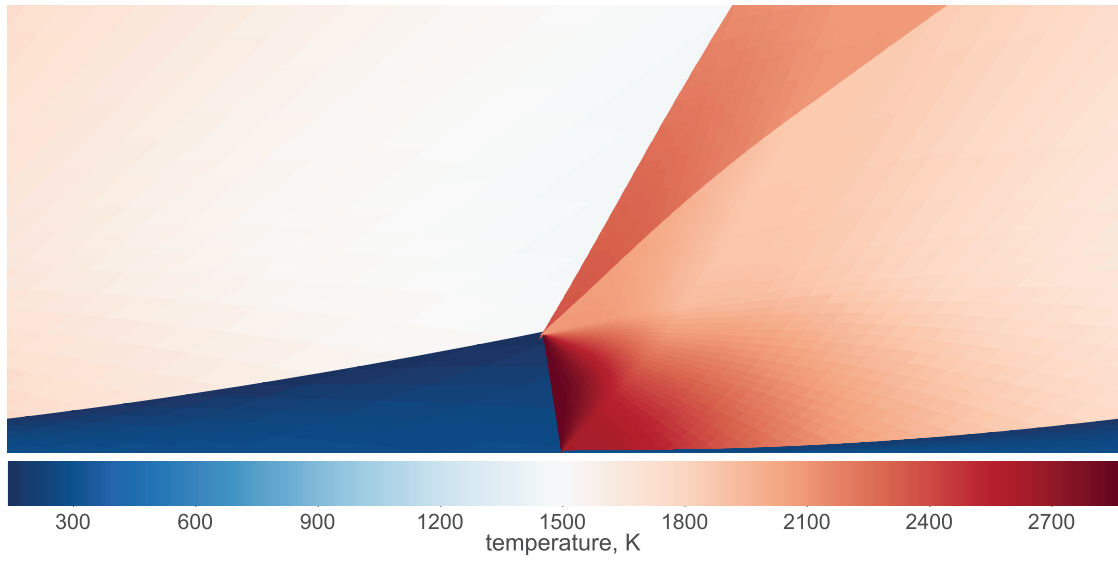
Figure 6.5: Temperature contours for $A_1/A_3 = 0.1$.
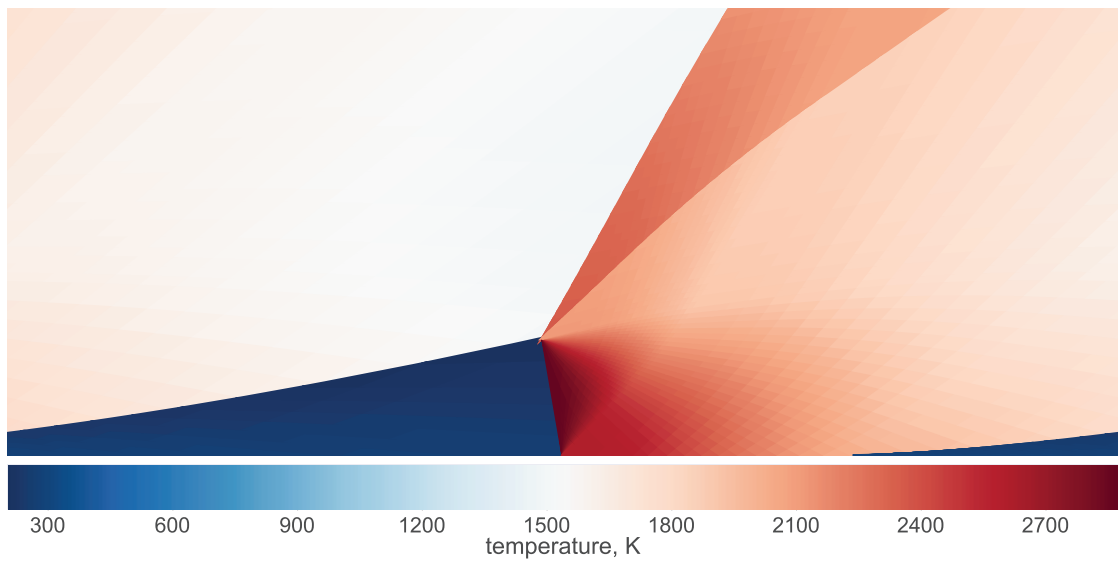
Figure 6.6: Temperature contours for $A_1/A_3 = 0.5$.
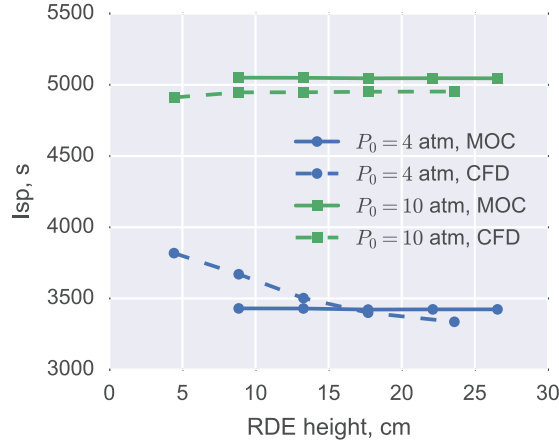
Figure 6.7: Effect of RDE annulus height on specific impulse for $l = 43.98$ cm, $w = 1$ cm, $A_1/A_3 = 0.2$, and $T_0 = 300$ K.

impulse [15] are shown in Fig. 6.7 for two values of the plenum stagnation pressure. The MOC model predicts that the RDE height has very little effect on performance, regardless of feed pressure. For the 10 atm case, the CFD and MOC model match fairly well. For the 4 atm case, however, the RDE height has an effect on performance that the MOC model does not predict. This difference is due to the boundary conditions at the exit of the RDE as well as limitations of the MOC model.

6.2 Limitations of MOC Modeling

The results from CFD simulations presented here use a mixed supersonic, subsonic boundary condition [46]. The MOC model does not have a boundary condition at the exit. Instead, the solution is marched out until it goes past the exit as shown in Fig. 5.1. Interpolation is then used to get the values at the exit boundary. For cases where the flow is supersonic in the vertical direction, there is generally no difference between the MOC and CFD solutions since no information

is required from beyond the exit to find the exit properties.

If all or part of the flow is subsonic in the vertical direction, information from beyond the RDE exit is required. In the CFD simulation, this is provided by the boundary condition in the form of a specified back pressure. The MOC model provides this information by using a portion of the solution that has been marched out past the exit. In effect, the MOC model is assuming that the RDE is larger than it actually is and ignoring any sort of geometry change that may occur at the exit. Figure 6.8 compares the vertical component of the exit Mach number for different RDE annulus heights.

Only the $P_0 = 4$ atm cases are shown, since the $P_0 = 10$ atm cases were nearly identical when comparing exit Mach number. For the 8.85 cm annulus height case, a portion of the exit flow is subsonic in the vertical direction. In the 26.55 cm case, all of the exit flow is supersonic in the vertical direction. The increase in annulus height gives the flow sufficient space to accelerate and turn, so that the vertical component of the exit Mach number is supersonic everywhere. This still does not fully describe why the $P_0 = 4$ atm case is more sensitive to annulus height than the $P_0 = 10$ atm case, since both cases have nearly identical exit Mach number profiles that depend almost entirely on annulus height. This leads to another issue with the boundary conditions, the specified back pressure.

The MOC solution ignores any imposed back pressure due to the hyperbolic nature of the method. The CFD exit boundary condition can and does impose a back pressure [46]. If the exit flow is supersonic in the vertical direction, but the pressure is less than the specified back pressure, the flow is overexpanded and has to
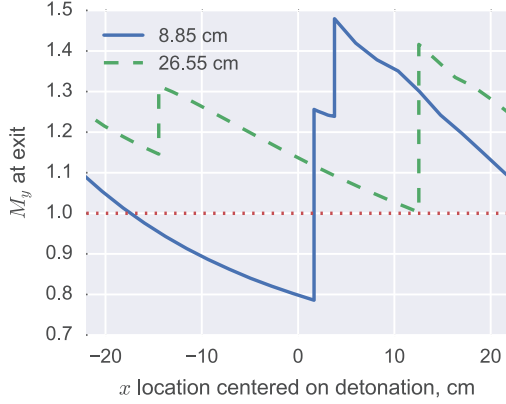
Figure 6.8: Vertical component of Mach number at the RDE exit for l = 43.98 cm, w = 1 cm, $A_1/A_3 = 0.2$, P_0 = 4 atm, and T_0 = 300 K.
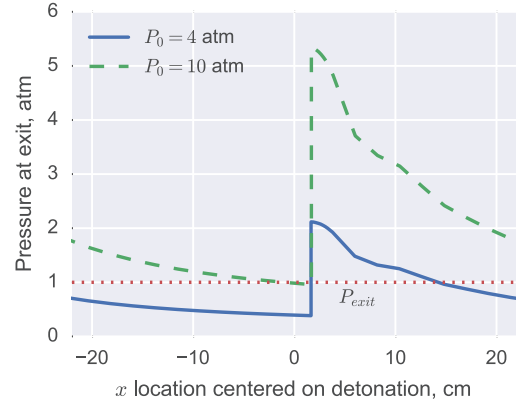
Figure 6.9: Exit pressure profiles for l = 43.98 cm, w = 1 cm, h = 8.85 cm, $A_1/A_3 = 0.2$, and T_0 = 300 K.

adjust so the pressures are matched. This adjustment may occur outside of the RDE annulus in the form of oblique shock waves for flows that are slightly overexpanded, or the shock waves may occur inside the annulus for highly overexpanded flows. If the adjustment occurs outside the annulus, the MOC and CFD solutions are the same. If the adjustment has to occur within the annulus, the MOC model is unable to adjust the flow and is effectively assuming a back pressure of zero so that the flow is always underexpanded.

The exit pressure profiles for the P_0 = 4 atm and P_0 = 10 atm cases are examined in Fig. 6.9. For P_0 = 4 atm, a majority of the flow is overexpanded, whereas for P_0 = 10 atm, nearly all of the flow is underexpanded. The fact that the flow is highly overexpanded for P_0 = 4 atm, in addition to there being a subsonic vertical component of the exit Mach number, is the most likely reason for the differences between the CFD and MOC solutions for low plenum feed pressures with short annulus heights.

6.3 Error Analysis
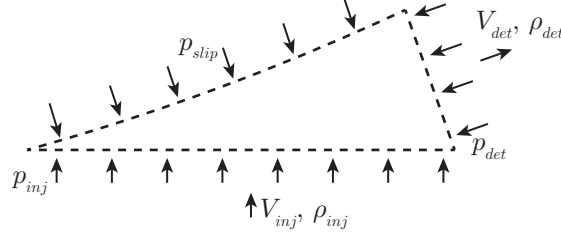
Figure 6.10: Control volume for the inflow region.

Errors are analyzed in two different ways. First, a control volume analysis of the inflow, post-detonation, and post-oblique shock regions is performed. Conservation of mass, momentum, and energy within these control volumes are examined on the basis of the number of starting characteristics along the initial value line in these regions. Second, the value of performance parameters such as specific impulse and thrust, are examined based on the resolution in all three regions. All of the following values are for the geometry and conditions used to generate Fig. 5.10.

The integral form of the Euler equations for steady flow are

$$\iint\limits_S \rho\mathbf{V}\cdot d\mathbf{S} = 0 \tag{6.4}$$

$$\iint\limits_S (\rho\mathbf{V}\cdot d\mathbf{S})\mathbf{V} + \iint\limits_S p d\mathbf{S} = 0 \tag{6.5}$$

$$\iint\limits_S \rho\left(e + \frac{V^2}{2}\right)\mathbf{V}\cdot d\mathbf{S} + \iint\limits_S p\mathbf{V}\cdot d\mathbf{S} = 0. \tag{6.6}$$

For the inflow region shown in Fig. 6.10, these equations become

$$-\int_{inj} \rho v dx + \int_{det} \rho(un_x + vn_y)ds = 0 \qquad (6.7)$$

$$-\int_{inj} \rho uv dx + \int_{det} [\rho(u^2 n_x + uvn_y) + pn_x]ds - \int_{slip} pdy = 0 \qquad (6.8)$$

$$-\int_{inj} (\rho v^2 + p)dx + \int_{det} [\rho(uvn_x + v^2 n_y) + pn_y]ds + \int_{slip} pdx = 0 \qquad (6.9)$$

$$-\int_{inj} \left[\rho v \left(e + \frac{V^2}{2}\right) + pv\right] dx + \int_{det} \left[\rho \left(e + \frac{V^2}{2}\right) + p\right] (un_x + vn_y)ds = 0. \qquad (6.10)$$

Similar equations can be generated for the post-detonation and post-oblique shock regions as well. Table 6.1 shows the % error in the mass, momentum, and energy fluxes into and out of the control volume. Note that as the resolution increases, the % error for the mass, momentum, and energy into and out of the control volume decreases. The inflow resolution was varied as the resolution in the post-detonation region was held constant with 20 starting characteristics from the top expansion fan and 10 starting characteristics from the bottom expansion fan. The post-oblique shock region was held with a constant resolution of 2 starting characteristics on the initial value line.

Table 6.1: Inflow region resolution study.

IVL resolution	Mass error	x-mom. error	y-mom. error	Energy error
5 points	0.835%	0.843%	0.259%	0.835%
10 points	0.377%	0.380%	0.300%	0.377%
20 points	0.128%	0.130%	0.0274%	0.128%
40 points	0.0110%	0.00549%	0.00808%	0.0110%
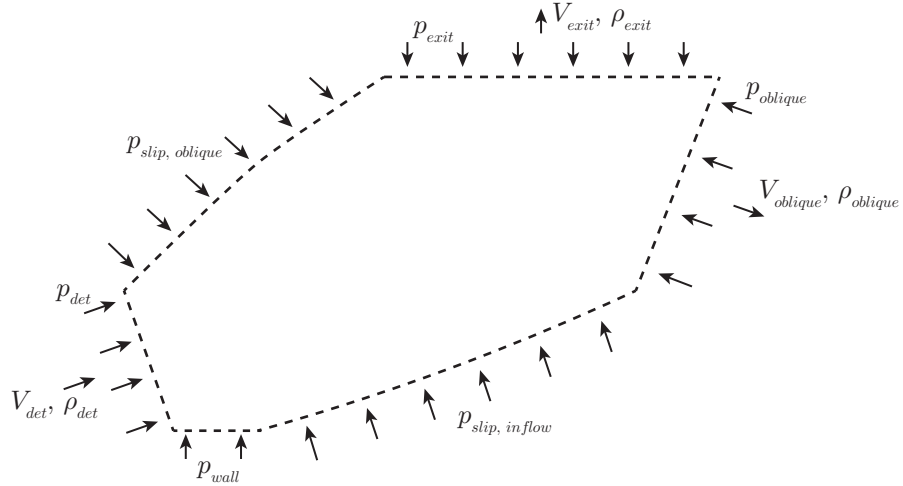
Figure 6.11: Control volume for the post-detonation region.

Figure 6.11 shows the control volume for the post-detonation region. Table 6.2 shows how the resolution in the post-detonation region affects conservation errors in that region. Note that the initial value line resolutions are set to 5 points in the inflow region and 2 points in the post-oblique shock region.

Table 6.2: Post-detonation region resolution study.

IVL res.	mass err.	x-mom. err.	y-mom. err.	energy err.	inflow region y-mom. err.
top: 20 bottom: 10	0.0932%	0.0939%	0.0991%	0.0935%	0.259%
top: 40 bottom: 20	0.0817%	0.0668%	0.0136%	0.0819%	0.0954%
top: 80 bottom: 40	0.00185%	0.00702%	0.0119%	0.00336%	0.0467%
top: 160 bottom: 80	0.0539%	0.0443%	0.00344%	0.04988%	0.000368%

Examining Table 6.2, as the resolution in increased, conservation errors decrease as expected until the last case. For the last case, the resolution in the post-

detonation region in very high while the resolution in the inflow and post-oblique shock regions is very low. For very high resolution cases, the resolution in the other regions must not be too low or errors along borders of the regions will dominate. Also shown in Table 6.2 is the error in the y-momentum in the inflow region as resolution is increased in the post-detonation region but held constant in the inflow region. Note that the errors in the inflow region decrease due to the increased resolution along the slip line between the inflow and post-detonation regions.

The odd behavior for the last case in Table 6.2 is examined by redoing the resolution study but increasing the resolution in the post-oblique shock region to 4 starting characteristics and increasing the resolution in the inflow region to 10 starting characteristics. The results of this study are shown in Table 6.3 and show that as the resolution is increased, errors generally decrease except for the y-momentum for the last case which is approximately the same as the previous case. Table 6.2 and 6.3 show that the errors present in each region can influence each other and that the resolution in each region should not vary greatly between different regions.
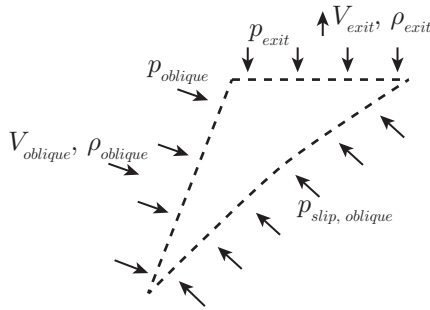

Figure 6.12: Control volume for the post-oblique shock region.

Lastly, Fig. 6.12 shows the control volume for the post-oblique shock region. Table 6.4 shows the change in conservation errors as the resolution is increased. The

70

Table 6.3: Post-detonation region resolution study for increased resolution in the inflow and post-oblique shock regions.

IVL res.	mass err.	x-mom. err.	y-mom. err.	energy err.
top: 20 bottom: 10	0.130%	0.0655%	0.156%	0.167%
top: 40 bottom: 20	0.0433%	0.0417%	0.0272%	0.0433%
top: 80 bottom: 40	0.0330%	0.0304%	0.00547%	0.0344%
top: 160 bottom: 80	0.00176%	0.000691%	0.00586%	0.00192%

resolution in both the inflow region and post-detonation region are held constant at the lowest resolutions in Tables 6.1 and 6.2. The errors decrease as the resolution is increased until the last case is reached which shows that the errors have stayed approximately constant between 8 and 16 starting characteristics. At this point, increased accuracy requires increasing the resolution in the post-detonation and inflow regions as well.

Table 6.4: Post-oblique region resolution study.

IVL resolution	Mass error	x-mom. error	y-mom. error	Energy error
2 points	0.277%	0.308%	0.177%	0.277%
4 points	0.0434%	0.0194%	0.0630%	0.0434%
8 points	0.0537%	0.0378%	0.0627%	0.0537%
16 points	0.0546%	0.0384%	0.0633%	0.0546%

In addition to examining conservation errors, a global resolution study is conducted to determine the dependence of calculated performance parameters on reso-
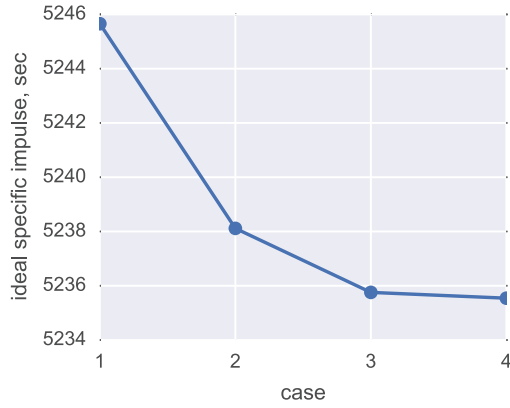
Figure 6.13: Specific impulse vs. resolution.
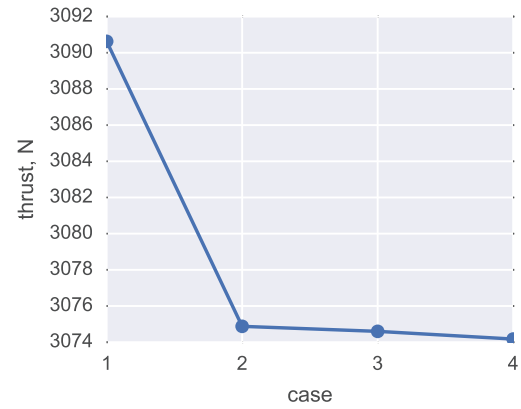
Figure 6.14: Thrust vs. resolution

lution. Four cases are studied where each case uses the resolutions in Tables 6.1, 6.2, and 6.4. For example, case 3 has a resolution of 20 points in the inflow region, 80 and 40 points in the post-detonation region for the top and bottom expansion fans, and 8 points in the post-oblique shock region. The results of this study are shown in Figs. 6.13 and 6.14. As the resolution is increased, the values of the specific impulse and thrust converge to an answer that changes little as the resolution is increased.

Chapter 7: Parametric Analysis of RDE Performance

The previously developed model is used to generate operation and performance data for a large parametric study. The goal of this study is identify and examine relationships found using dimensional analysis. This analysis is used to generate scaling laws for RDEs.

The ideal RDE model developed previously has many parameters that may be adjusted and examined. For a constant γ, constant molecular weight detonation model, these parameters are:

- w, width

- c, circumference

- A_{inj}, injector area

- h, height

- P_0, plenum pressure

- ρ_0, plenum density

- q, heat release

- c_p, specific heat capacity at constant pressure

73

- c_v, specific heat capacity at constant volume

- P_b, back pressure

The following sections will examine these parameters to find which are important depending on the metric of interest and which can be ignored. A dimensional analysis is also performed to reduce the number of cases and help shed light on the important relationships when determining RDE performance. Simplified relationships based on the dimensional analysis and parametric study are created to aid in future RDE design efforts.

7.1   Analysis of RDE Height

This section deals with the height of the RDE annulus. As seen previously in Fig. 6.7, the annulus height was shown to have no effect on specific impulse. The effect of height is examined in greater detail in Figs. 7.1, 7.2, 7.3, and 7.4 (diameter: 15 cm, width: 1 cm, A_t/A_c: 0.3, γ: 1.3, MW: 22.0 g/mol, q: 3.5 MJ/kg, P_b: 1 atm, T_0: 300 K). All of the figures show that the annulus height has little to no effect on the thrust, mass flow rate, pre-detonation pressure, or pre-detonation temperature. This is shown at plenum pressures of 10, 15, and 20 atm. Figure 7.4 also shows that neither annulus height or plenum pressure has an effect on pre-detonation temperature.

The equation to calculate the exit thrust is given by

$$F = \int_{exit} [\rho v^2 + (P - P_b)]dA. \tag{7.1}$$

74
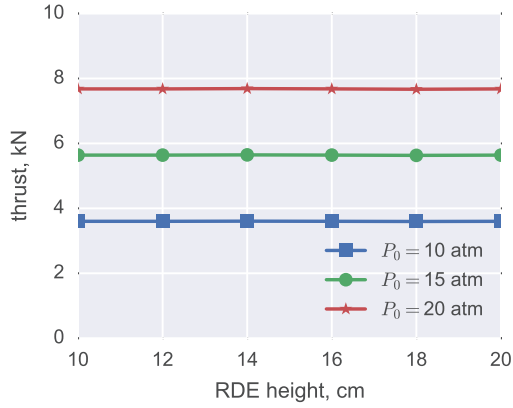
Figure 7.1: Thrust vs. annulus height.
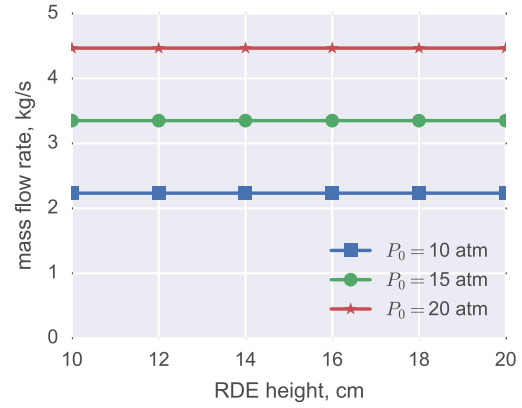
Figure 7.2: Mass flow rate vs. annulus height.
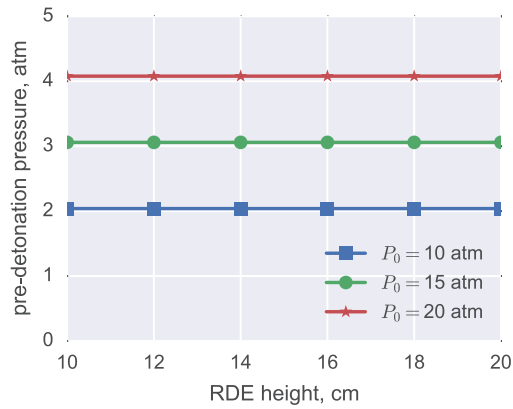
Figure 7.3: Pre-detonation pressure vs. annulus height.

Figure 7.4: Pre-detonation temperature vs annulus height.

Figures 7.5 and 7.6 shows the exit profiles for the ρv^2 and $(P - P_b)$ terms at annulus heights of 10, 15, and 20 cm for a plenum pressure of 10 atm. As the height of the annulus increases, the profiles for both ρv^2 and $(P - P_b)$ see a decrease in the maximum amplitude and a broadening of the profiles. Additionally, the integrated value of ρv^2 is increasing as the height increases and the integrated value of $(P - P_b)$ decreases so that the sum is constant and equal to the thrust.
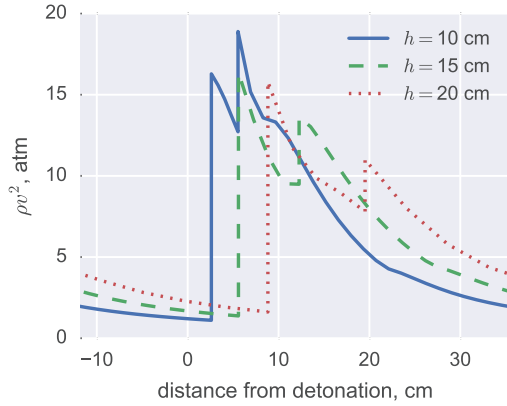
Figure 7.5: ρv^2 exit profiles for various annulus heights.
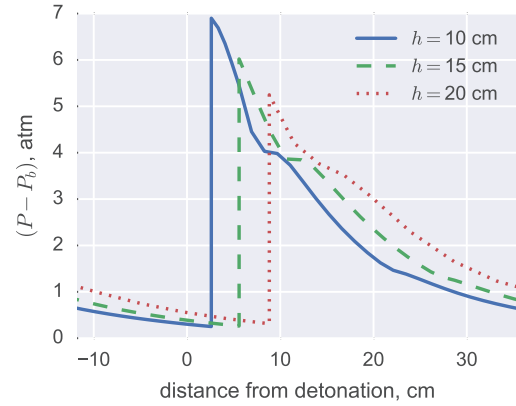
Figure 7.6: $(P - P_b)$ exit profiles for various annulus heights.

7.2 Analysis of RDE Diameter and Channel Width

The effect of the RDE diameter on thrust, mass flow rate, pre-detonation pressure, and pre-detonation temperature is shown in Figs. 7.7, 7.8, 7.9, and 7.10, respectively, for an RDE with a 1 cm wide annular channel. It can be seen that the thrust and mass flow rate scale linearly with diameter. The pre-detonation pressure and temperature are not affected by the RDE diameter.

The effects of channel width are similar to that of the RDE diameter. This may be seen in Figs. 7.11, 7.12, 7.13, and 7.14 for an RDE with a constant diameter of 15 cm. Note that as either the diameter or channel width is increased, the channel area is also increasing. By scaling the thrust and mass flow rate with channel area instead of diameter or width, the results from the diameter and width studies lie on the same line. The cases where the plenum pressure is held at 10 atm are shown in Figs. 7.15 and 7.16. These figures show that the thrust and mass flow rate scale linearly with the channel area. The dimensional analysis given later may now only
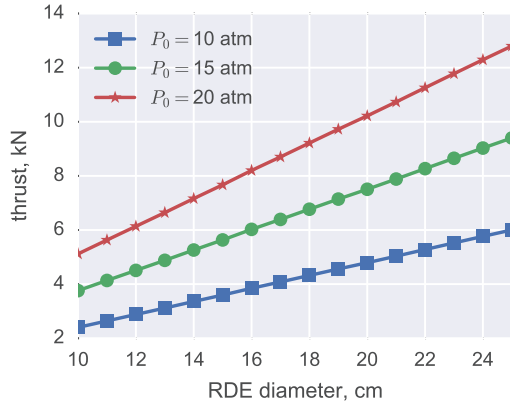
Figure 7.7: Thrust vs. annulus diameter.
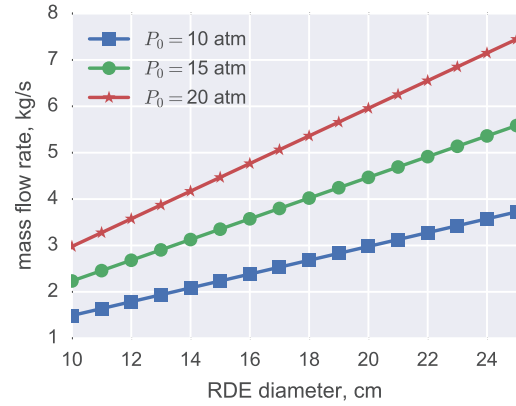
Figure 7.8: Mass flow rate vs. annulus diameter.
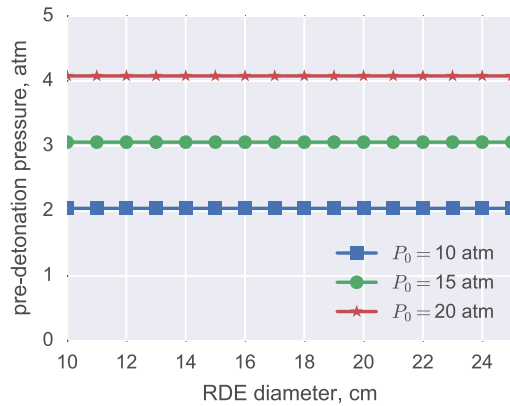
Figure 7.9: Pre-detonation pressure vs. annulus diameter.
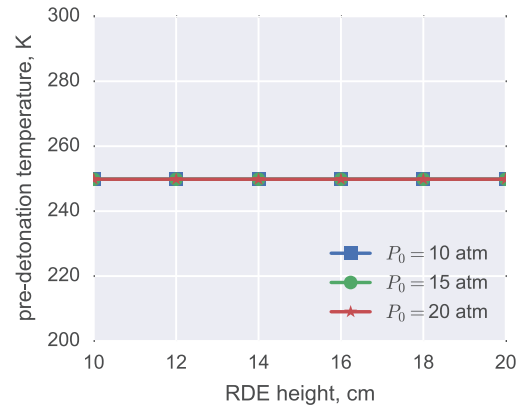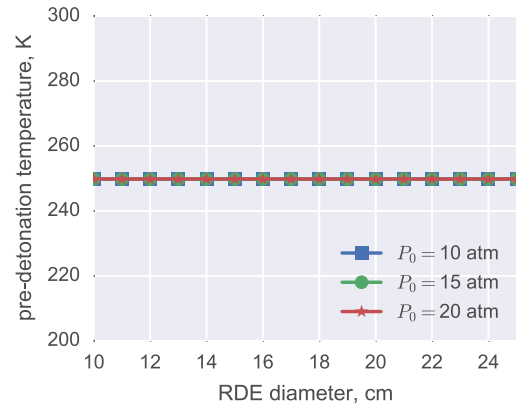

Figure 7.10: Pre-detonation temperature vs annulus diameter.

take into account the channel area and not the diameter and width allowing the analysis to be simplified.

Use of the channel area instead of the diameter or width is only valid when examining the thrust, mass flow rate, pre-detonation pressure, and pre-detonation temperature. The thrust and mass flow rate scale linearly with channel area and the pre-detonation pressure and pre-detonation temperature are affected by the channel area through the injector to channel area ratio which is shown in a later section. However; when examining the axial detonation height, the diameter becomes an important parameter. Figures 7.17 and 7.18 show the effect of RDE diameter and
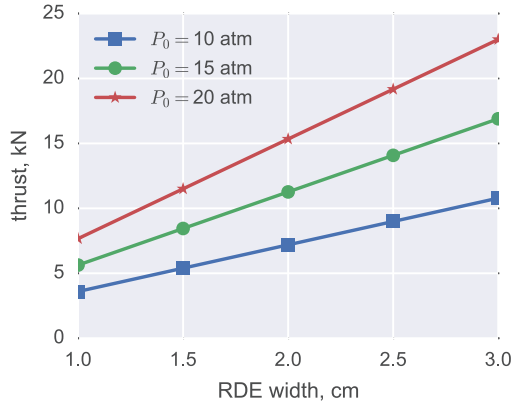
Figure 7.11: Thrust vs. annulus width.
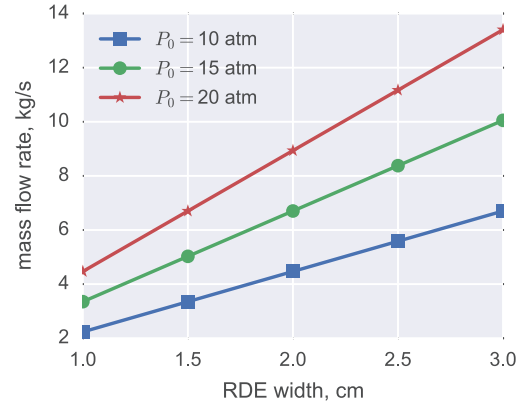
Figure 7.12: Mass flow rate vs. annulus width.
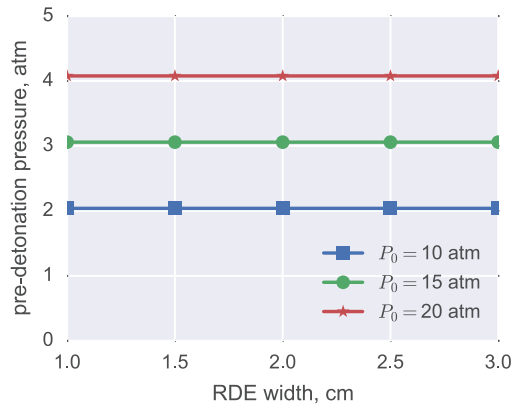
Figure 7.13: Pre-detonation pressure vs. annulus width.
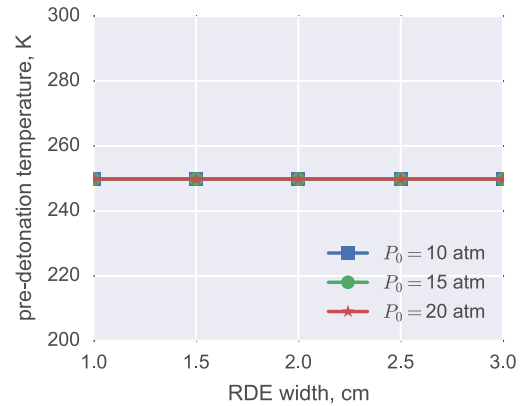
Figure 7.14: Pre-detonation temperature vs annulus width.

width on the axial detonation height. The detonation height scales linearly with the diameter but the channel width has no effect. It is interesting to note that even though the detonation height may be changing, the pre-detonation pressure and pre-detonation temperature (which are averaged quantities) remain constant.

7.3 Dimensional Analysis

Using the channel area instead of the width and diameter as well as ignoring the annulus height, reduces the number of parameters from 10 to 8. Since there
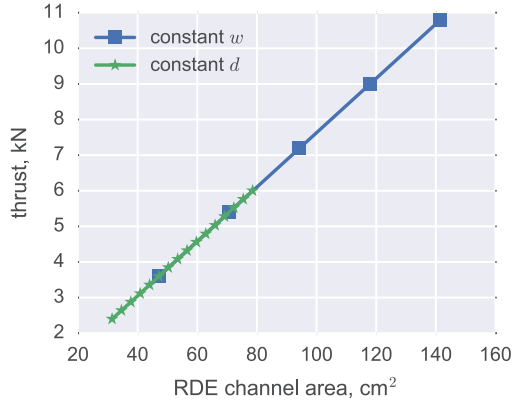
Figure 7.15: Thrust vs. channel area.
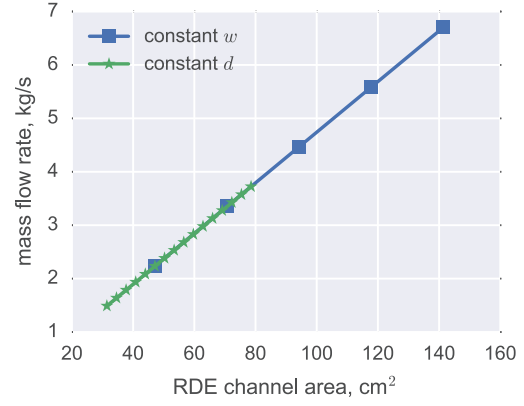
Figure 7.16: Mass flow rate vs. channel area.
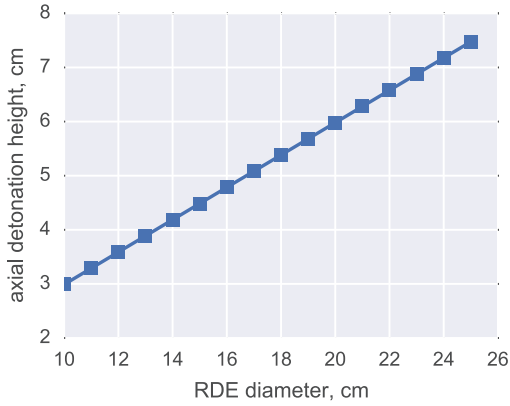
Figure 7.17: Axial detonation height vs. RDE diameter.
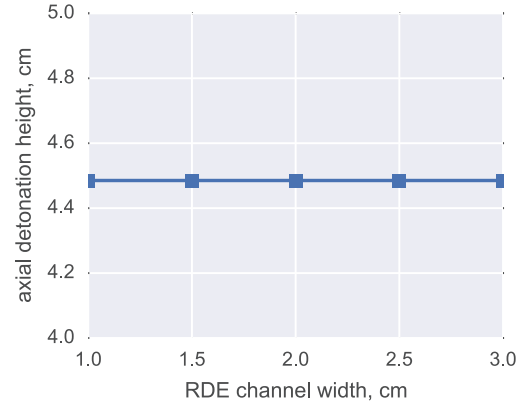
Figure 7.18: Axial detonation height vs. channel width.

are four fundamental dimensions (mass, length, time, and temperature), dimensional analysis may further reduce this number by 4. This leaves 4 non-dimensional parameters to explore instead of 8. The non-dimensional groupings are:

$$\Pi_1 = AR = \frac{A_{inj}}{A_{channel}} \tag{7.2}$$

$$\Pi_2 = Q = \frac{q}{P_0 \nu_0} \tag{7.3}$$

$$\Pi_3 = \frac{P_b}{P_0} \tag{7.4}$$

$$\Pi_3 = \gamma. \tag{7.5}$$

79

They represent the injector-to-channel area ratio, the non-dimensional heat release, the pressure ratio across the RDE, and the ratio of specific heats. Note that the pressure ratio across the RDE, $\Pi_3 = P_b/P_0$, only affects the thrust calculation. This is due to the inability of exit conditions to affect the flow within the RDE. This limitation is discussed in a previous chapter.

7.4 Analysis of Thrust

The thrust is non-dimensionalized by dividing by the plenum pressure multiplied by the channel area:

$$\Pi_0 = \frac{F}{P_0 A_c}. \tag{7.6}$$

The functional relationship for the non-dimensional thrust may now be written as

$$\frac{F}{P_0 A_c} = f\left(\frac{A_t}{A_c}, \frac{q}{P_0 \nu_0}, \frac{P_b}{P_0}, \gamma\right). \tag{7.7}$$

The variation of the non-dimensional thrust with the area ratio while holding the non-dimensional heat release constant is shown in Fig. 7.19. In Fig. 7.19, $P_b/P_0 = 0.1$ and $\gamma = 1.3$. The RDE diameter and height are both 15 cm. There is an approximately linear relationship between the area ratio and non-dimensional thrust. As the non-dimensional heat release is increased, the non-dimensional thrust also increases. This may also be seen in Fig. 7.20 which shows the relationship between the non-dimensional thrust and non-dimensional heat release. The non-dimensional heat release is varied by changing the plenum temperature, heat release, and molecular weight. The cases are shown in Table 7.1.
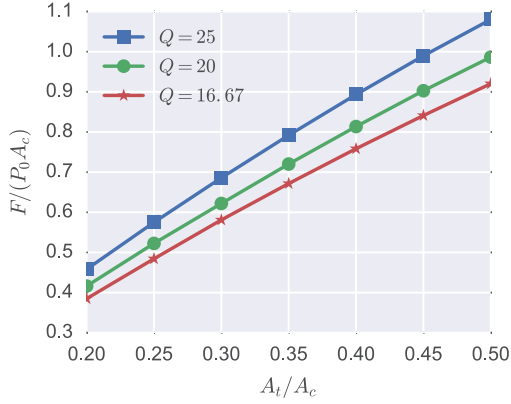
Figure 7.19: Non-dimensional thrust vs. area ratio.
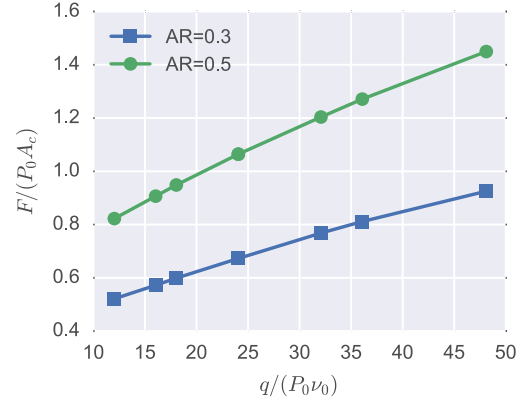
Figure 7.20: Non-dimensional thrust vs. non-dimensional heat release.

Table 7.1: Cases for non-dimensional heat release study.

Case	T_0, K	q, MJ/kg	MW g/mol	$q/(P_0\nu_0)$
1	300.0	3.0	20.0	24.1
2	300.0	3.0	30.0	36.1
3	300.0	4.0	20.0	32.1
4	300.0	4.0	30.0	48.1
5	600.0	3.0	20.0	12.0
6	600.0	3.0	30.0	18.1
7	600.0	4.0	20.0	16.0
8	600.0	4.0	30.0	24.1

The effect of the ratio of specific heats on non-dimensional thrust is shown in Figs. 7.21 and 7.22. For these figures, P_b/P_0=0.1 and $Q = 25$. As the ratio of specific heats in increased, the non-dimensional thrust increases. Lastly, the effect of the pressure ratio, P_b/P_0, across the RDE is examined in Fig. 7.23. As the pressure ratio decreases, the non-dimensional thrust increases due to the decreased back pressure.
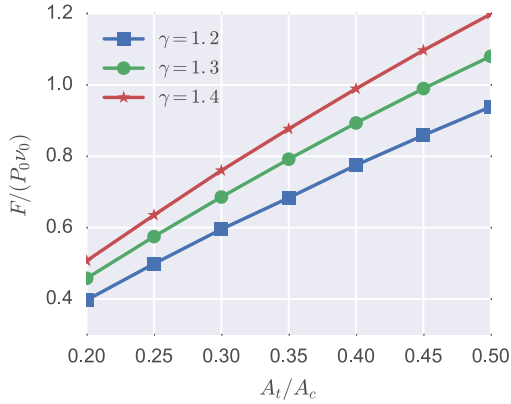
Figure 7.21: Non-dimensional thrust vs. area ratio with various values of γ.
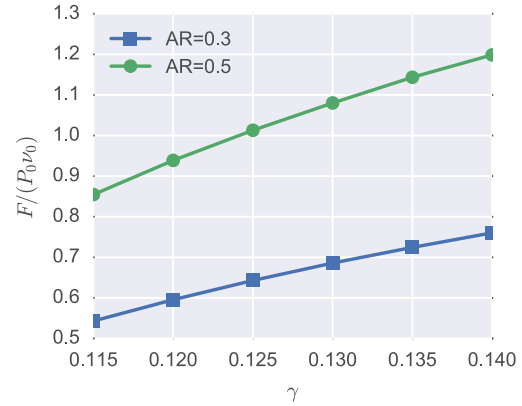
Figure 7.22: Non-dimensional thrust vs. the ratio of specific heats.
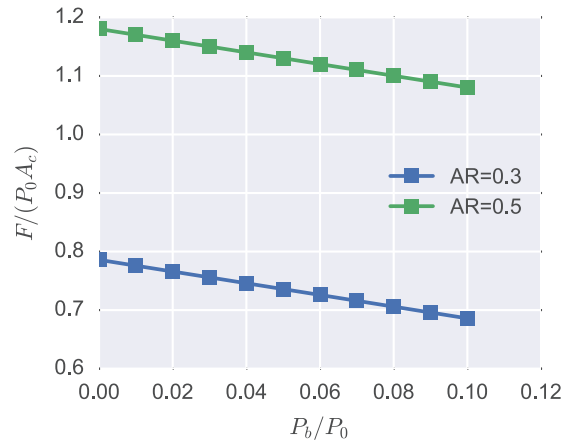
Figure 7.23: Non-dimensional thrust vs. the pressure ratio, P_b/P_0.

7.5 Analysis of Pre-Detonation Conditions

The averaged pressure and temperature in front of the detonation wave are required to estimate detonation wave speeds and detonability. The pre-detonation conditions are non-dimensionalized by dividing by the plenum conditions. This leads

to the following relationships for the non-dimensional pressure and temperature:

$$\frac{P_{det}}{P_0} = f\left(\frac{A_t}{A_c}, \frac{q}{P_0 \nu_0}, \gamma\right) \tag{7.8}$$

$$\frac{T_{det}}{T_0} = f\left(\frac{A_t}{A_c}, \frac{q}{P_0 \nu_0}, \gamma\right). \tag{7.9}$$

Starting with the pre-detonation pressure, Figs. 7.24 and 7.25 show the influence of the area ratio, non-dimensional heat release, and specific heat capacity ratio on the pre-detonation pressure. The area ratio has the largest influence on the pre-detonation pressure. The non-dimensional heat release parameter has very little effect and may be ignored when developing a relationship to estimate the pressure. The ratio of specific heats has a noticeable effect but it is not as important as the area ratio effect.
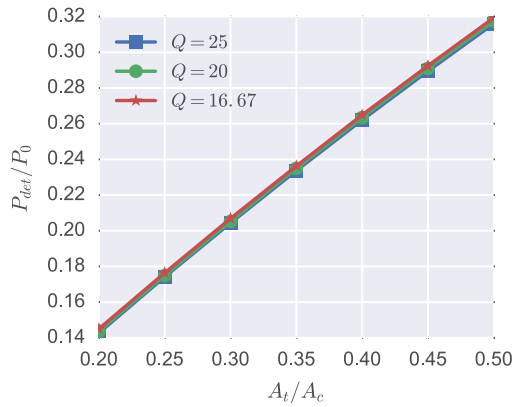
Figure 7.24: Non-dimensional pre-detonation pressure vs. area ratio with various values of Q.
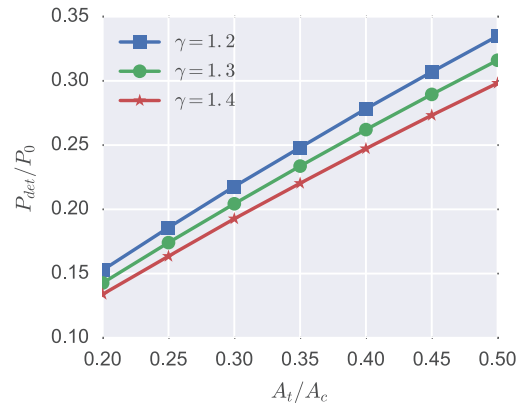
Figure 7.25: Non-dimensional pre-detonation pressure vs. area ratio with various values of γ.

The pre-detonation temperature behaves similarly to the pre-detonation pressure. Figure 7.26 shows how the pre-detonation temperature changes with the area ratio and the non-dimensional heat release. The main effect is with the area ratio. The non-dimensional heat release has very little effect. Figure 7.27 examines the ef-

fect of area ratio and the ratio of specific heats. The ratio of specific heats has a very noticeable effect that cannot be ignored when determining the pre-detonation temperature. Lastly, it is important to note that the non-dimensional pre-detonation temperature does not vary that much due to the area ratio. The largest changes are due to the ratio of specific heats.
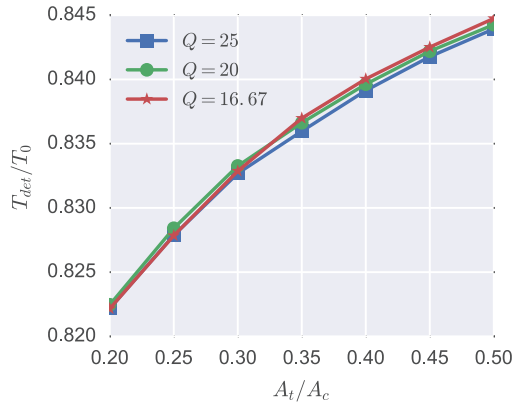
Figure 7.26: Non-dimensional pre-detonation temperature vs. area ratio with various values of Q.
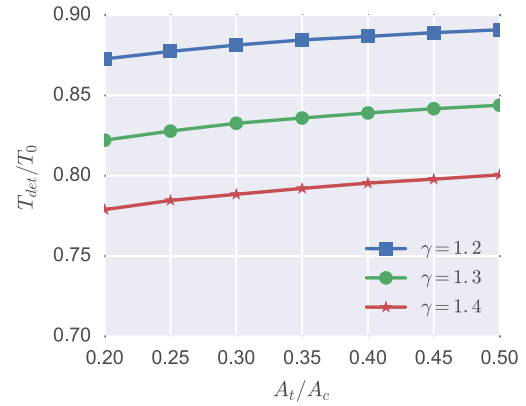
Figure 7.27: Non-dimensional pre-detonation temperature vs. area ratio with various values of γ.

7.6 Analysis of Mass Flow Rate

The mass flow rate is non-dimensionalized as

$$\Pi_0 = \frac{\dot{m}}{\sqrt{P_0 \rho_0} A_t}. \tag{7.10}$$

The functional relationship for the non-dimensional mass flow may now be written as

$$\frac{\dot{m}}{\sqrt{P_0 \rho_0} A_t} = f\left(\frac{A_t}{A_c}, \frac{q}{P_0 \nu_0}, \gamma\right). \tag{7.11}$$

The effect of the area ratio, non-dimensional heat release, and the ratio of specific heats is shown in Figs. 7.28 and 7.29. The area ratio has the largest impact on the

non-dimensional mass flow rate. The non-dimensional heat release also has a small effect. The ratio of specific heats appears to have an effect that is more pronounced at larger area ratios and decreases as the area ratio decreases.
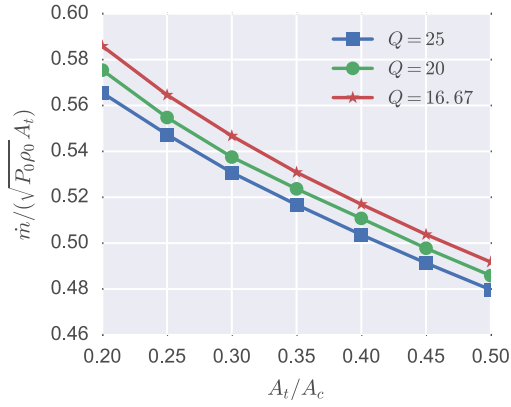
Figure 7.28: Non-dimensional mass flow rate vs. area ratio with various values of Q.
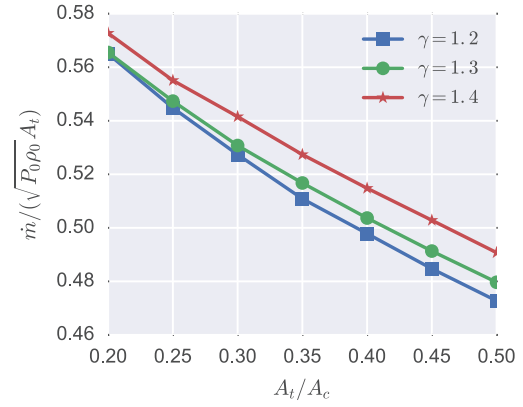
Figure 7.29: Non-dimensional mass flow rate vs. area ratio with various values of γ.

It is sometimes useful to calculate the mass flow rate using the one-dimensional mass flow equation

$$\dot{m} = \frac{A_t P_0}{\sqrt{T_0}} \sqrt{\frac{\gamma}{R}} M_1 \left(1 + \frac{\gamma - 1}{2} M_1^2 \right)^{-(\gamma+1)/(2(\gamma-1))}. \tag{7.12}$$

If the flow is choked, this reduces to

$$\dot{m} = \frac{A_t P_0}{\sqrt{T_0}} \sqrt{\frac{\gamma}{R}} \left(\frac{\gamma + 1}{2} \right)^{-(\gamma+1)/(2(\gamma-1))}. \tag{7.13}$$

This is an easy way to calculate the mass flow rate. Unfortunately, the flow across the injectors in an RDE may be blocked, unchoked, or choked. To simplify the mass flow calculation, it is useful to define an effective injector area, A_t^*, which is the are that would recover the correct mass flow rate in an RDE. It is now possible to define a blockage ratio,

$$B = 1 - \frac{A_t^*}{A_t}, \tag{7.14}$$

which defines the fractional amount of the injector area that is blocked by the high pressure of the detonation. This does not represent the actual area blocked. The blockage ratio represents the fraction of the injector area to subtract in order for a choked flow calculation to recover the correct mass flow through an RDE. The blockage ratio is a simple to use and easy to understand concept that may be used when estimating the mass flow rate through an RDE.

The functional relationship for the blockage ratio is

$$B = f\left(\frac{A_t}{A_c}, \frac{q}{P_0\nu_0}, \gamma\right). \tag{7.15}$$

The effect of the area ratio, non-dimensional heat release, and ratio of specific heats is shown in Figs. 7.30 and 7.31. The blockage ratio follows similar trends that are flipped from the non-dimensional mass flow rate.
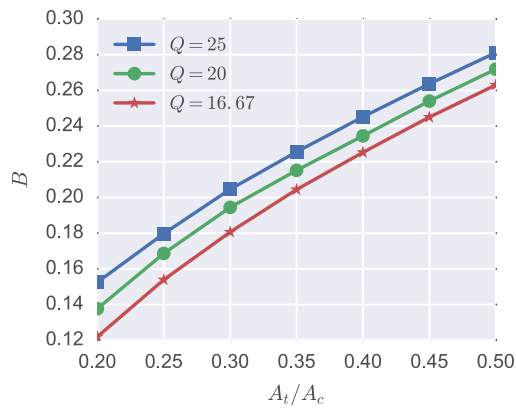
Figure 7.30: Blockage ratio vs. area ratio with various values of Q.
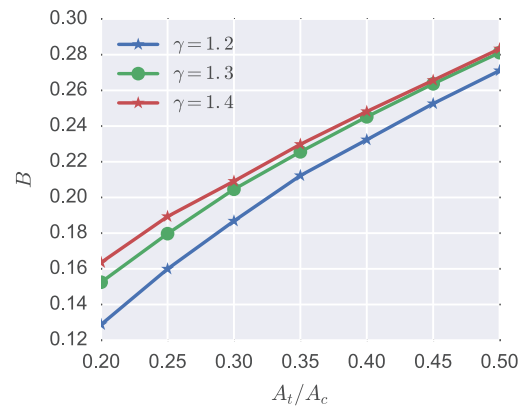
Figure 7.31: Blockage ratio vs. area ratio with various values of γ.

Chapter 8: Conclusions

8.1   Concluding Remarks

Current analyses of the RDE flowfield are done using unsteady numerical simulations in the laboratory frame. After several cycles, the solutions generally reach a quasi-steady state. This is computationally expensive since the solution must be run until an averaged solution is found. An additional drawback to traditional CFD is the requirement to model the detonation wave. Generally, this requires the use of a chemically reacting flow model with enough resolution to resolve the reaction zone behind the detonation.

The method of characteristics allows for a quick, steady-state analysis of stable RDE operation. Additionally, a planar CJ approximation of the detonation wave may be employed to remove the difficulty of modeling a detonation in two-dimensions. Another simplification comes in the form of assuming the composition is frozen on either side of the detonation wave. There are also drawbacks to this approach. First, implementation of the method of characteristics is complex and great care must be taken to implement the boundary conditions and treat discontinuities in the flowfield correctly. Another drawback is assuming a steady-state solution even though detonation waves are an inherently unsteady phenomena. Regardless

of these drawbacks, it has been shown that the MOC model is capable of providing useful performance predictions on par with conventional Euler simulations and at significantly less computational cost.

This approach to generating RDE flowfields was developed so that an engineer may perform large-scale parametric studies without having to rely entirely on simplified one-dimensional models or computationally expensive CFD simulations. Unlike one-dimensional models, the MOC model is capable of modeling the curved oblique shock wave, exit swirl, counter-flow, detonation inclination, and varying pressure along the inflow boundary. While not as fast as a one-dimensional model, the MOC model is still fast enough for large-scale parametric studies. Once a design space has been found, high-fidelity numerical simulations may then be used to examine additional effects on the flowfield. There is also work being done to determine if the MOC solution may be used to initialize a CFD simulation, which would decrease the amount of time spent in the starting transient phase. The work presented here bridges the gap between very simple one-dimensional models and high-fidelity CFD simulations and gives the researcher another tool for understanding RDE flow processes.

8.2   Summary of Contributions

- Developed a novel method for modeling RDE flowfields that uses the method of characteristics to calculate performance information at significantly reduced computational costs compared to traditional numerical simulations.

- Developed an analytical description of the detonation-oblique shock interaction. This work was based on previously developed models for detonation-inert gas interactions.

- Developed a new, first-of-its-kind boundary condition for the method of characteristics to simulate mass injection.

- Extended the mass-entropy method to handle flows with large entropy gradients. This new method, called the mass-stagnation method, is also capable of handling non-constant freestream conditions ahead of an oblique shock wave.

- Developed a new interpolation methodology based on the method of characteristics to provide enhanced accuracy in low resolution regions of the characteristic mesh.

- Showed that the new MOC method predicts performance to within several percent of far more expensive CFD simulations.

- Explored the limitations of the MOC method as well as the effect of characteristic mesh resolution.

- Conducted a large parametric study to determine which parameters play important roles in determining the thrust, mass flow rate, and averaged pre-detonation conditions. The most important parameters were the injector-to-channel area ratio and non-dimensional heat release parameter.

- Showed that the key dimensionless parameters governing an RDE's performance are the injector-to-channel area ratio, the non-dimensional heat release,

the ratio of specific heats, and the pressure ratio between the plenum and back pressures.

8.3 Future Work

Future work should focus on improving the reduced order model to handle additional physics missing in the current model. These may be grouped into three categories dealing with the boundary conditions, MOC formulations, and detonation modeling. A list of future improvements with the reduced order model follows:

- Inflow boundary condition - 1) ability to handle backflow in to the injection system and 2) ability to handle different injector geometries.

- Outflow boundary conditions - 1) ability to impose a specified back pressure and 2) ability to handle a sudden contraction or throat.

- Nozzled RDEs - use the quasi-2D Euler equations with area change in the axial direction to estimate the effect of area change through the annular combustor.

- Equilibrium and finite rate chemistry - use equilibrium MOC or finite rate MOC to model the effects of equilibrium or finite rate chemistry on RDE performance.

- Detonation modeling - ability to model the detonation to get the correct shape and global velocity based on the gradients ahead of the detonation. This model should also be able to correctly determine the post-detonation flow properties and gradients as well so that averaging is no longer required.

Appendix A: Unit Processes

The unit processes listed here are based on the predictor-corrector algorithms given in [75]. The main difference is the use of the mass-stagnation method to perform the streamline calculations in order to increase accuracy. Additionally, in [75], the compatibility equations along a streamline are solved numerically. Since the model developed here assumes a calorically perfect gas, these equations have a closed form solution that is used in place of the numerical approximation. As shown in section 4.1, Eqs. 4.8 and 4.9 may be replaced with the definition of the stagnation pressure and stagnation density along a streamline.

Finite difference equations are only needed for the characteristic and compatibility equations along the Mach lines. The characteristic and compatibility equations along the streamline are handled by the mass-stagnation method. For the predictor-corrector algorithm described in [75], the finite difference form of the characteristic and compatibility equations along the Mach lines are

$$\Delta y_\pm = \lambda_\pm \Delta x_\pm \tag{A.1}$$

$$Q_\pm \Delta P_\pm \pm \Delta \theta_\pm = 0, \tag{A.2}$$

respectively, where $\lambda_\pm$ is defined as

$$\lambda_\pm = \tan(\theta \pm \mu) \tag{A.3}$$

and where $Q_{\pm}$ is defined as

$$Q_{\pm} = \frac{\sqrt{M^2 - 1}}{\rho V^2}. \qquad (A.4)$$

Equation A.1 is used to solve for the location of a point where the characteristics intersect and Eq. A.2 is used to solve for the pressure and flow angle at that point. Next, the mass integral is calculated through an iterative process using the trapezoidal rule described in section 4.2. With the value of the mass integral known, the value of the stagnation pressure and stagnation density along the streamline is known. This allows for the calculation of the density and velocity. More detail about the actual implementation is given in the following sections.

A.1 Interior Point Unit Process

The interior point unit process is the most often called unit process and provides the most basic illustration of the MOC algorithm used to simulate RDE flowfields. A detailed overview given here will apply to most other unit processes required to generate a full RDE solution. An illustration is shown in Fig. A.1. In Fig A.1, a right-running characteristic emanating from point 1 is intersecting a left-running characteristic emanating from point 2 to create point 4. In order to solve for the state
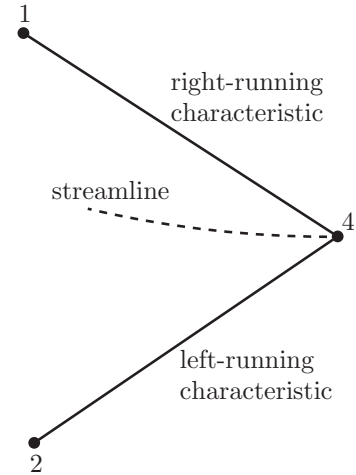
Figure A.1: Illustration of an interior point unit process.

and location of point 4, information from the streamline going through point 4 is also required in addition to information from points 1 and 2.

Equation A.2 is the finite difference equation for the compatibility relation along the characteristics. For the interior point unit process, it may be written as

$$Q_+ P_4 + \theta_4 = T_+ \tag{A.5}$$

$$Q_- P_4 - \theta_4 = T_- \tag{A.6}$$

where

$$T_+ = Q_+ P_2 + \theta_2 \tag{A.7}$$

$$T_- = Q_- P_1 - \theta_1. \tag{A.8}$$

For the predictor step, only information from points 1 and 2 are used to calculate Q_+ and Q_-:

$$Q_+ = \frac{\sqrt{M_2^2 - 1}}{\rho_2 V_2^2} \tag{A.9}$$

$$Q_- = \frac{\sqrt{M_1^2 - 1}}{\rho_1 V_1^2}. \tag{A.10}$$

Solving this finite difference equation gives an estimate of the pressure and flow angle at point 4. To estimate the location of point 4 for the predictor step, Eq. A.1 is written as

$$y_4 - \lambda_+ x_4 = y_2 - \lambda_+ x_2 \tag{A.11}$$

$$y_4 - \lambda_- x_4 = y_1 - \lambda_- x_1 \tag{A.12}$$

where λ_+ and λ_- are estimated only using information at points 2 and 1, respectively. They are given by:

$$\lambda_+ = \tan\left(\theta_2 + \mu_2\right) \tag{A.13}$$

$$\lambda_- = \tan\left(\theta_1 - \mu_1\right). \tag{A.14}$$

Once P_4, θ_4, x_4, and y_4 have been estimated, the mass-stagnation method is used to get ρ_4 and V_4 through an iterative process. To start the iterative process, P_{0_4} and ρ_{0_4} are guessed to be the average values between points 1 and 2. Once the stagnation values are known, the definitions given in Eqs. 4.14 and 4.15 are used to calculate ρ_4 and V_4. Using θ_4 and V_4, u_4 and v_4 are calculated as

$$u_4 = V_4 \cos(\theta_4) \tag{A.15}$$

$$v_4 = V_4 \sin(\theta_4). \tag{A.16}$$

The next step is to calculate the value of the mass integral using the trapezoidal rule (Eq. 4.21). It is possible to calculate ψ_4 going from either point 1 or point 2 using

$$\psi_{4_+} = \psi_1 + (x_1 - x_4)\left(\frac{\rho_1 v_1 + \rho_4 v_4}{2}\right) - (y_1 - y_4)\left(\frac{\rho_1 u_1 + \rho_4 u_4}{2}\right) \tag{A.17}$$

$$\psi_{4_-} = \psi_2 + (x_2 - x_4)\left(\frac{\rho_2 v_2 + \rho_4 v_4}{2}\right) - (y_2 - y_4)\left(\frac{\rho_2 u_2 + \rho_4 u_4}{2}\right). \tag{A.18}$$

The current implementation calculates the mass integral both ways and takes the average. Once ψ_4 is known, it is used to linearly interpolate for P_{0_4} and ρ_{0_4} using look-up tables defined at a boundary that relates the mass integral to the stagnation pressure and stagnation density. The new values for the stagnation pressure and stagnation density are used to calculate ρ_4 and V_4 and the process is repeated until a convergence criteria is met. In this algorithm, the criteria is that the change in stagnation pressure between iterations falls below a defined error tolerance.

After completion of the predictor step, the corrector step begins for either a specified number of iterations or until a convergence criteria is met. The algorithm

presented here performs the corrector step until an error tolerance is met. Since there are now estimates as to the state and location of point 4; Q_+, Q_-, λ_+, and λ_- are all calculated using the average property method described in [75]. The average property method averages P, θ, V, and ρ along the characteristics. The finite difference coefficients then become

$$Q_+ = \frac{\sqrt{M_+^2 - 1}}{\rho_+ V_+^2} \tag{A.19}$$

$$Q_- = \frac{\sqrt{M_-^2 - 1}}{\rho_- V_-^2} \tag{A.20}$$

$$\lambda_+ = \tan(\theta_+ + \mu_+) \tag{A.21}$$

$$\lambda_- = \tan(\theta_- - \mu_-) \tag{A.22}$$

where V_+, θ_+, V_-, and θ_- are averages between points 2 and 4 and 1 and 4, respectively. The values for M_+, μ_+, M_- and μ_- are computed using the average properties as well. New values of P_4, θ_4, x_4, and y_4 are now calculated using Q_+, Q_-, λ_+, and λ_-. After this, the iterative mass-stagnation process is started using the previously calculated values of P_{0_4} and ρ_{0_4} and proceeds as described above to calculate new values of ρ_4 and V_4. With updated values at point 4, the corrector step is repeated until the difference in P_4 between iterations is below a specified tolerance.

The pseudocode for the interior point unit process is given in A.1. It has been broken up among several algorithms to illustrate the main steps used. The algorithm gives an organized view of the method described above.

Algorithm A.1 Interior point unit process

Require: ratio of specific heats, γ
Require: x, y, V, θ, ρ, P, and ψ for points 1 and 2
Require: look-up tables: $\boldsymbol{\psi}$, $\boldsymbol{P_0}$, $\boldsymbol{\rho_0}$
    Comment: perform predictor step
1: calculate a, M, μ, u, v, P_0, and ρ_0 for points 1 and 2
2: calculate finite difference coefficients $\triangleright$ algorithm A.2
3: calculate P_4, θ_4, x_4, and y_4 $\triangleright$ algorithm A.4
4: $P_{0_4} = \text{average}(P_{0_1}, P_{0_2})$
5: $\rho_{0_4} = \text{average}(\rho_{0_1}, \rho_{0_2})$
6: calculate ρ_4, V_4 using mass-stagnation method $\triangleright$ algorithm A.6
    Comment: perform corrector step
7: **while** $|error| > tolerance$ **do**
8:     calculate averaged properties along Mach lines $\triangleright$ algorithm A.5
9:     calculate finite difference coefficients $\triangleright$ algorithm A.3
10:     calculate P_4, θ_4, x_4, and y_4 $\triangleright$ algorithm A.4
11:     calculate ρ_4, V_4 using mass-stagnation method $\triangleright$ algorithm A.6
12:     $error = P_{4,old} - P_4$
13: **end while**
14: return x_4, y_4, V_4, θ_4, ρ_4, P_4, and ψ_4

Algorithm A.2 Calculate finite difference coefficients for predictor step
---
1: $\lambda_+ = \tan(\theta_2 + \mu_2)$
2: $Q_+ = \frac{\sqrt{M_2^2 - 1}}{\rho_2 V_2^2}$
3: $T_+ = Q_+ P_2 + \theta_2$
4: $\lambda_- = \tan(\theta_1 - \mu_1)$
5: $Q_- = \frac{\sqrt{M_1^2 - 1}}{\rho_1 V_1^2}$
6: $T_- = Q_- P_1 - \theta_1$

Algorithm A.3 Calculate finite difference coefficients for corrector step
---
1: $\lambda_+ = \tan(\theta_+ + \mu_+)$
2: $Q_+ = \frac{\sqrt{M_+^2 - 1}}{\rho_+ V_+^2}$
3: $T_+ = Q_+ P_2 + \theta_2$
4: $\lambda_- = \tan(\theta_- - \mu_-)$
5: $Q_- = \frac{\sqrt{M_-^2 - 1}}{\rho_- V_-^2}$
6: $T_- = Q_- P_1 - \theta_1$

Algorithm A.4 Calculate P_4, θ_4, x_4, and y_4

1: $P_4 = \frac{T_+ + T_-}{Q_+ + Q_-}$
2: $\theta_4 = P_4 Q_- - T_-$
3: $x_4 = \frac{y_2 - \lambda_+ x_2 - y_1 + \lambda_- x_1}{\lambda_- - \lambda_+}$
4: $y_4 = y_1 - \lambda_- x_1 + \lambda_+ x_4$

Algorithm A.5 Average property method

1: $P_+ = \text{average}(P_2, P_4)$
2: $\theta_+ = \text{average}(\theta_2, \theta_4)$
3: $V_+ = \text{average}(V_2, V_4)$
4: $\rho_+ = \text{average}(\rho_2, \rho_4)$
5: calculate a_+, M_+, μ_+ using + values
6: $P_- = \text{average}(P_1, P_4)$
7: $\theta_- = \text{average}(\theta_1, \theta_4)$
8: $V_- = \text{average}(V_1, V_4)$
9: $\rho_- = \text{average}(\rho_1, \rho_4)$
10: calculate a_-, M_-, μ_- using $-$ values

Algorithm A.6 Mass-stagnation method

1: **while** $|error| > tolerance$ **do**
2:     calculate M_4 ▷ from Eq. 4.14
3:     calculate ρ_4 ▷ from Eq. 4.15
4:     calculate V_4, u_4, v_4
5:     $\psi_{4_-} = \psi_1 + (x_1 - x_4)\left(\frac{\rho_1 v_1 + \rho_4 v_4}{2}\right) - (y_1 - y_4)\left(\frac{\rho_1 u_1 + \rho_4 u_4}{2}\right)$
6:     $\psi_{4_+} = \psi_2 + (x_2 - x_4)\left(\frac{\rho_2 v_2 + \rho_4 v_4}{2}\right) - (y_2 - y_4)\left(\frac{\rho_2 u_2 + \rho_4 u_4}{2}\right)$
7:     $\psi_4 = \text{average}(\psi_{4_+}, \psi_{4_-})$
8:     $P_{0_4} = \text{interpolate}(\boldsymbol{P_0}, \boldsymbol{\psi}, \psi_4)$
9:     $\rho_{0_4} = \text{interpolate}(\boldsymbol{\rho_0}, \boldsymbol{\psi}, \psi_4)$
10:     $error = P_{0_{4,old}} - P_{0_4}$
11: **end while**
12: calculate ρ_4 and V_4 with new values of P_{0_4} and ρ_{0_4}

A.2   Inflow Point Unit Process

The inflow point unit process does not exist in the literature and had to be developed in order to model mass injection into the RDE annulus. The analytical equations that form the basis of this model are given in section 3.3. The MOC boundary condition using these equations is described in section 4.3. A more in depth description of how the inflow unit process works is presented here.
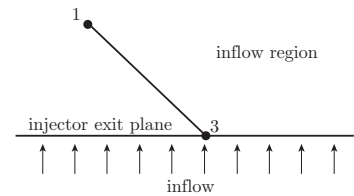
Figure A.2: Illustration of a inflow point unit process.

The inflow point unit process is similar to the oblique shock unit process described in [75]. Instead of solving the oblique shock relations, the relations describing a flow undergoing a sudden expansion are used. An illustration of the inflow unit process is shown in Fig. **??**. In this illustration, a right-running characteristic from point 1 is hitting the mass injection boundary at point 3. The compatibility relation along the characteristic is

$$\frac{\sqrt{M^2 - 1}}{\rho V^2} dp_- - d\theta_- = 0. \tag{A.23}$$

The equations describing the inflow process at point 3 are

$$\dot{m} = \frac{A_i P_0}{\sqrt{T_0}} \sqrt{\frac{\gamma}{R}} \left(1 + \frac{\gamma - 1}{2} M_1^2\right)^{-(\gamma+1)/(2(\gamma-1))} \tag{A.24}$$

$$\frac{1}{2} v_3^2 + \frac{\gamma}{\gamma - 1} \frac{P_3 A_c}{\dot{m}} v_3 - \frac{\gamma}{\gamma - 1} \frac{P_0}{\rho_0} = 0 \tag{A.25}$$

$$P_2 = \frac{\dot{m}(v_3 - v_1) - P_1 A_i + P_3 A_c}{A_c - A_i} \tag{A.26}$$

$$u_3 = u_{ref} \tag{A.27}$$

$$\theta = \tan^{-1}\left(\frac{v_3}{u_3}\right). \tag{A.28}$$

The solution procedure is to find the correct P_3 and θ_3 to satisfy both the compatibility relation and inflow equations simultaneously. The easiest way to accomplish this is through the use of a nonlinear equation solver. Algorithm A.7 shows the system to plug into a nonlinear equation solver that will then satisfy both the inflow and compatibility relations for the inflow point unit process.

Algorithm A.7 System for inflow point unit process

Require: guess for the pressure at point 3, P_3

Require: fluid parameters, γ and R

Require: plenum properties, P_0, T_0, and ρ_0

Require: reference frame velocity, u_{ref}

Require: x, y, V, θ, ρ, and P at point 1

Require: injector and channel areas, A_i and A_c

    Comment: perform injector calculation

1: calculate v_3, T_3, and $\dot{m}$ using Eqs. A.24, A.25, and A.26

2: $\rho_3 = P_3/(RT_3$

3: $V_3 = \sqrt{u_{ref}^2 + v_3^2}$

4: $\theta_3 = \tan^{-1}(v_3/u_{ref})$

    Comment: compatibility relation using average property method

5: $P_- = \text{average}(P_1, P_3)$

6: $V_- = \text{average}(V_1, V_3)$

7: $\rho_- = \text{average}(\rho_1, \rho_3)$

8: calculate a_- and M_- using averaged values

9: $Q_- = \frac{\sqrt{M_-^2-1}}{\rho_-V_-^2}$

10: $T_- = Q_-P_1 - \theta_1$

11: $P_{4,new} = \frac{T_-+\theta_3}{Q_-}$

12: residual $= P_4 - P_{4,new}$

13: return residual

Bibliography

[1] William H Heiser and David T Pratt. Thermodynamic cycle analysis of pulse detonation engines. *Journal of Propulsion and Power*, 18(1):68–76, 2002.

[2] Fedor A Bykovskii, Sergey A Zhdan, and Evgenii F Vedernikov. Continuous spin detonations. *Journal of Propulsion and Power*, 22(6):1204–1216, 2006.

[3] BV Voitsekhovskii. Maintained detonations. In *Soviet Physics Doklady*, volume 4, page 1207, 1960.

[4] K Kailasanath. The rotating-detonation-wave engine concept: A brief status report. In *49th AIAA Aerospace Sciences Meeting*, AIAA Paper 2011-580, Jan. 2011.

[5] Piotr Wolański. Detonative propulsion. *Proceedings of the Combustion Institute*, 34(1):125–158, 2013.

[6] Frank K Lu and Eric M Braun. Rotating detonation wave propulsion: experimental challenges, modeling, and engine concepts. *Journal of Propulsion and Power*, 30(5):1125–1142, 2014.

[7] Ya B Zeldovich. To the question of energy use of detonation combustion. *Zh. Tech. Fiz*, 10(17):1453–1461, 1940.

[8] K Kailasanath. Research on pulse detonation combustion systems–a status report. In *47th AIAA Aerospace Sciences Meeting*, AIAA Paper 2009-631, Jan. 2009.

[9] Andrew Naples. Recent progress in detonation at air force research labs. In *International Workshop on Detonation for Propulsion*, Busan, Korea, 2011.

[10] Eric Wintenberger and Joseph E Shepherd. Stagnation hugoniot analysis for steady combustion waves in propulsion systems. *Journal of propulsion and power*, 22(4):835–844, 2006.

[11] SA Ashford and G Emanuel. Oblique detonation wave engine performance prediction. *Journal of propulsion and power*, 12(2):322–327, 1996.

[12] John HS Lee. *The detonation phenomenon*, volume 2. Cambridge University Press Cambridge, 2008.

[13] JA Nicholls, RE Cullen, and KW Ragland. Feasibility studies of a rotating detonation wave rocket motor. *Journal of Spacecraft and Rockets*, 3(6):893–898, 1966.

[14] Piotr Wolański. Detonation engines. *Journal of KONES*, 18:515–521, 2011.

[15] Douglas A Schwer and Kailas Kailasanath. Numerical study of the effects of engine size on rotating detonation engines. In *49th AIAA Aerospace Sciences Meeting*, AIAA Paper 2011-581, Jan. 2011.

[16] FA Bykovskii and VV Mitrofanov. Detonation combustion of a gas mixture in a cylindrical chamber. *Combustion, Explosion, and Shock Waves*, 16(5):570–578, 1980.

[17] FA Bykovskii, AA Vasil'ev, EF Vedernikov, and VV Mitrofanov. Explosive combustion of a gas mixture in radial annular chambers. *Combustion, Explosion and Shock Waves*, 30(4):510–516, 1994.

[18] FA Bykovskii and EF Vedernikov. Continuous detonation combustion of an annular gas-mixture layer. *Combustion, explosion, and shock waves*, 32(5):489–491, 1996.

[19] FA Bykovskii, VV Mitrofanov, and EF Vedernikov. Continuous detonation combustion of fuel-air mixtures. *Combustion, Explosion and Shock Waves*, 33(3):344–353, 1997.

[20] FA Bykovskii, SA Zhdan, and EF Vedernikov. Spin detonation of fuel-air mixtures in a cylindrical combustor. In *Doklady Physics*, volume 50, pages 56–58. Springer, 2005.

[21] FA Bykovskii, SA Zhdan, and EF Vedernikov. Continuous spin detonation in annular combustors. *Combustion, Explosion and Shock Waves*, 41(4):449–459, 2005.

[22] FA Bykovskii, SA Zhdan, and EF Vedernikov. Continuous spin detonation of fuel-air mixtures. *Combustion, Explosion and Shock Waves*, 42(4):463–471, 2006.

[23] FA Bykovskii, SA Zhdan, and EF Vedernikov. Continuous spin detonation of hydrogen-oxygen mixtures. 1. annular cylindrical combustors. *Combustion, Explosion, and Shock Waves*, 44(2):150–162, 2008.

[24] FA Bykovskii, SA Zhdan, and EF Vedernikov. Continuous spin detonation of hydrogen-oxygen mixtures. 2. combustor with an expanding annular channel. *Combustion, Explosion, and Shock Waves*, 44(3):330–342, 2008.

[25] FA Bykovskii and EF Vedernikov. Continuous spin detonation of hydrogen-oxygen mixtures. 3. methods of measuring flow parameters and flow structure in combustors of different geometries. *Combustion, Explosion, and Shock Waves*, 44(4):451–460, 2008.

[26] FA Bykovskii, SA Zhdan, and EF Vedernikov. Realization and modeling of continuous spin detonation of a hydrogen-oxygen mixture in flow-type combustors. 1. combustors of cylindrical annular geometry. *Combustion, Explosion, and Shock Waves*, 45(5):606–617, 2009.

[27] FA Bykovskii, SA Zhdan, and EF Vedernikov. Realization and modeling of continuous spin detonation of a hydrogen-oxygen mixture in flow-type combustors. 2. combustors with expansion of the annular channel. *Combustion, Explosion, and Shock Waves*, 45(6):716–728, 2009.

[28] FA Bykovskii, SA Zhdan, and EF Vedernikov. Continuous detonation in the regime of nonstationary ejection of the oxidizer. In *Doklady Physics*, volume 54, pages 29–31. Springer, 2009.

[29] FA Bykovskii, SA Zhdan, and EF Vedernikov. Continuous detonation in the air ejection mode. domain of existence. *Combustion, Explosion, and Shock Waves*, 47(3):330–334, 2011.

[30] FA Bykovskii, SA Zhdan, and EF Vedernikov. Continuous detonation in the regime of self-oscillatory ejection of the oxidizer. 1. oxygen as a oxidizer. *Combustion, Explosion, and Shock Waves*, 46(3):344–351, 2010.

[31] FA Bykovskii, SA Zhdan, and EF Vedernikov. Continuous detonation in the regime of self-oscillatory ejection of the oxidizer. 2. air as an oxidizer. *Combustion, Explosion, and Shock Waves*, 47(2):217–225, 2011.

[32] FA Bykovskii, SA Zhdan, and EF Vedernikov. Reactive thrust generated by continuous detonation in the air ejection mode. *Combustion, Explosion, and Shock Waves*, 49(2):188–195, 2013.

[33] FA Bykovskii, SA Zhdan, and EF Vedernikov. Continuous spin detonation of a hydrogen-air mixture with addition of air into the products and the mixing region. *Combustion, Explosion, and Shock Waves*, 46(1):52–59, 2010.

[34] FA Bykovskii. Thermal fluxes in combustion chamber walls in the detonation and turbulent combustion modes. *Combustion, Explosion, and Shock Waves*, 27(1):66–71, 1991.

[35] FA Bykovskii and EF Vedernikov. Heat fluxes to combustor walls during continuous spin detonation of fuel-air mixtures. *Combustion, Explosion, and Shock Waves*, 45(1):70–77, 2009.

[36] FA Bykovskii, EF Vedernikov, and SV Polozov. Noise and vibrations in a combustor with continuous spin detonation combustion of the fuel. *Combustion, Explosion and Shock Waves*, 42(5):582–593, 2006.

[37] FA Bykovskii, EF Vedernikov, SV Polozov, and Yu V Golubev. Initiation of detonation in flows of fuel-air mixtures. *Combustion, Explosion, and Shock Waves*, 43(3):345–354, 2007.

[38] Andrew Naples, John Hoke, James Karnesky, and Fred Schauer. Flowfield characterization of a rotating detonation engine. In *51st AIAA Aerospace Sciences Meeting including the New Horizons Forum and Aerospace Exposition, AIAA Paper*, number 2013-0278, 2013.

[39] Rachel M Russo, Paul I King, Fred Schauer, and Levi M Thomas. Characterization of pressure rise across a continuous detonation engine. In *Joint Propulsion Conference*, 2011.

[40] Levi M Thomas, Frederick R Schauer, John L Hoke, and Andrew Naples. Buildup and operation of a rotating detonation engine. In *49th AIAA Aerospace Sciences Meeting including the New Horizons Forum and Aerospace Exposition*, volume 4, 2011.

[41] Richard Dyer, Andrew Naples, Thomas Kaemming, John Hoke, and Fred Schauer. Parametric testing of a unique rotating detonation engine design. In *50th AIAA Aerospace Sciences Meeting including the New Horizons Forum and Aerospace Exposition*, pages 9–12, 2012.

[42] S Theuerkauf, Fred Schauer, Richard Anthony, and John Hoke. Average and instantaneous heat release to the walls of an rde. In *52nd AIAA Aerospace Sciences Meeting, AIAA*, volume 1503, page 2014, 2014.

[43] B Rankin, John Hoke, and Fred Schauer. Periodic exhaust flow through a converging-diverging nozzle downstream of a rotating detonation engine. In *52nd AIAA Aerospace Sciences Meeting, AIAA Paper*, number 2014-1015, 2014.

[44] J Kindracki, P Wolański, and Z Gut. Experimental research on the rotating detonation in gaseous fuels–oxygen mixtures. *Shock waves*, 21(2):75–84, 2011.

[45] BL Naour, F Falempin, and F Miquel. Recent experimental results obtained on continuous detonation wave engine. In *17th AIAA International Space Planes and Hypersonic Systems and Technologies Conference*, 2011.

[46] Douglas A Schwer and Kailas Kailasanath. Numerical investigation of rotating detonation engines. In *46th AIAA/ASME/SAE/ASEE Joint Propulsion Conference and Exhibit*, AIAA Paper 2010-6880, Jul. 2010.

103

[47] Manabu Hishida, Toshi Fujiwara, and Piotr Wolanski. Fundamentals of rotating detonations. *Shock waves*, 19(1):1–10, 2009.

[48] Tae-Hyeong Yi, Jing Lou, Cary Turangan, Jeong-Yeol Choi, and Piotr Wolanski. Propulsive performance of a continuously rotating detonation engine. *Journal of Propulsion and Power*, 27(1):171–181, 2011.

[49] Douglas A Schwer and K Kailasanath. Effect of inlet on fill region and performance of rotating detonation engines. In *47th Joint Propulsion Conference*, AIAA Paper 2011-6044, 2011.

[50] Douglas A Schwer and Kailas Kailasanath. Feedback into mixture plenums in rotating detonation engines. In *50th AIAA Aerospace Sciences Meeting*, AIAA Paper 2012-0617, 2012.

[51] Douglas A Schwer and K Kailasanath. On reducing feedback pressure in rotating detonation engines. In *51st AIAA Aerospace Sciences Meeting*, AIAA Paper 2013-1178, 2013.

[52] SA Zhdan, FA Bykovskii, and EF Vedernikov. Mathematical modeling of a rotating detonation wave in a hydrogen-oxygen mixture. *Combustion, explosion, and shock waves*, 43(4):449–459, 2007.

[53] SA Zhdan. Mathematical model of continuous detonation in an annular combustor with a supersonic flow velocity. *Combustion, Explosion, and Shock Waves*, 44(6):690–697, 2008.

[54] Dmitry M Davidenko, Iskender Gokalp, and Alexey N Kudryavtsev. Numerical study of the continuous detonation wave rocket engine. In *15th AIAA International Space Planes and Hypersonic Systems and Technologies Conference*, AIAA Paper 2008-2680, 2008.

[55] Dmitry M Davidenko, Yohann Eude, Iskender Gökalp, and François Falempin. Theoretical and numerical studies on continuous detonation wave engines. In *17th AIAA International Space Planes and Hypersonic Systems and Technologies Conference*, AIAA Paper 2011-2334, 2011.

[56] Tae-Hyeong Yi, Jing Lou, Cary Turangan, Boo Cheong Khoo, and Piotr Wolanski. Effect of nozzle shapes on the performance of continuously rotating detonation engine. In *48th AIAA Aerospace Sciences Meeting*, AIAA Paper 2010-152, 2010.

[57] Craig A Nordeen, Douglas Schwer, Fredrick Schauer, John Hoke, B Cetegen, and T Barber. Divergence and mixing in a rotating detonation engine. In *51st AIAA Aerospace Sciences Meeting*, 2013.

[58] SA Zhdan and AS Syryamin. Numerical modeling of continuous detonation in non-stoichiometric hydrogen-oxygen mixtures. *Combustion, Explosion, and Shock Waves*, 49(1):69–78, 2013.

[59] Douglas A Schwer and Kailas Kailasanath. Towards non-premixed injection modeling of rotating detonation engines. In *51st AIAA/SAE/ASEE Joint Propulsion Conference*, 2015.

[60] C Towery, K Smith, Prateek Shrestha, Peter E Hamlington, and Marthinus Van Schoor. Examination of turbulent flow effects in rotating detonation engines. In *44th AIAA Fluid Dynamics Conference*, 2014.

[61] Tae-Hyeong Yi, Cary Turangan, Jing Lou, Piotr Wolanski, and Jan Kindracki. A three-dimensional numerical study of rotational detonation in an annular chamber. In *47th AIAA Aerospace Sciences Meeting*, AIAA Paper 2009-634, 2009.

[62] Douglas A Schwer and Kailas Kailasanath. Modeling exhaust effects in rotating detonation engines. In *48th Joint Propulsion Conference*, AIAA Paper 2012-3943, 2012.

[63] D Schwer, A Corrigan, and K Kailasanath. Towards efficient, unsteady, three-dimensional rotating detonation engine simulations. In *52nd AIAA Aerospace Sciences Meeting*, 2014.

[64] CA Nordeen, D Schwer, F Schauer, J Hoke, Th Barber, and B Cetegen. Thermodynamic model of a rotating detonation engine. *Combustion, Explosion, and Shock Waves*, 50(5):568–577, 2014.

[65] Tom Kaemming, Matthew Fotia, John Hoke, and Frederick Schauer. Thermodynamic modeling of a rotating detonation engine through a reduced order approach. In *54th AIAA Aerospace Sciences Meeting*, AIAA Paper 2016-1405, Jan. 2016.

[66] Andrew R Mizener and Frank K Lu. Preliminary parametric analysis of a rotating detonation engine by analytical methods. In *52nd AIAA/SAE/ASEE Joint Propulsion Conference*, page 4876, 2016.

[67] D Paxson. Numerical analysis of a rotating detonation engine in the relative reference frame. In *52nd AIAA Aerospace Sciences Meeting*, AIAA Paper 2014-0284, Jan. 2014.

[68] Eliahou Khedhoory Dabora, JA Nicholls, and RB Morrison. The influence of a compressible boundary on the propagation of gaseous detonations. In *Symposium (International) on Combustion*, volume 10, pages 817–830. Elsevier, 1965.

[69] William P Sommers and Richard B Morrison. Simulation of condensed-explosive detonation phenomena with gases. *The Physics of Fluids*, 5(2):241–248, Feb. 1962.

[70] Martin Sichel and JC Foster. The ground impulse generated by a plane fuel-air explosion with side relief. *Acta Astronautica*, 6(3):243–256, 1979.

[71] Toshiataka Fujiwara and Shun-ichi Tsuge. Quasi-onedimensional analysis of gaseous free detonations. *Journal of the Physical Society of Japan*, 33(1):237–241, 1972.

[72] Vadim N Gamezo, Takanobu Ogawa, and Elaine S Oran. Numerical simulations of flame propagation and ddt in obstructed channels filled with hydrogen–air mixture. *Proceedings of the Combustion Institute*, 31(2):2463–2471, 2007.

[73] S Brown and JE Shepherd. Numerical solution methods for shock and detonation jump conditions. galcit report fm 2006.006, 2004.

[74] David G. Goodwin, Harry K. Moffat, and Raymond L. Speth. Cantera: An object-oriented software toolkit for chemical kinetics, thermodynamics, and transport processes. http://www.cantera.org, 2015. Version 2.2.0.

[75] Maurice J Zucrow and Joe D Hoffman. *Gas dynamics. Volume 2-Multidimensional flow*. New York: John Wiley and Sons, Inc., 1977.

[76] SA Powers and JB Oneill. Determination of hypersonic flow fields by the method of characteristics. *AIAA Journal*, 1(7):1693–1694, 1963.

[77] Daniel E Paxson and Jack Wilson. An improved numerical model for wave rotor design and analysis. In *31st AIAA Aerospace Sciences Meeting*, AIAA Paper 1993-0482, Jan. 1992.

[78] Philip A Thompson. *Compressible-fluid dynamics*. New York: McGraw-Hill, 1971.

[79] John David Anderson. *Modern compressible flow: with historical perspective*, volume 3. McGraw-Hill New York, 1990.

[80] NA Cumpsty and JH Horlock. Averaging nonuniform flow for a purpose. *Journal of Turbomachinery*, 128(1):120–129, 2006.